Microstructural Characterization of a 4043 Al Alloy Produced by Molten Metal Deposition (MMD)

St Peter's College



A thesis submitted for the degree of master by research at the University of Oxford

Mingji Dai
Supervisors: Enzo Liotti and Patrick S. Grant

Abstract

Additive manufacturing (AM) encompasses a range of layer-by-layer fabrication techniques that have transformed modern manufacturing by enabling the production of complex geometries, reducing material waste, and offering unprecedented design flexibility. These advantages have made AM particularly attractive for industries such as aerospace, automotive and biomedical engineering. However, despite its growing adoption, conventional AM approaches—particularly powder- and laser-based processes—face several limitations, including high equipment and material costs, energy-intensive operation, and challenges related to process stability, residual stresses and microstructural control. In this context, molten metal deposition (MMD) has emerged as a promising wire-fed AM variant in which liquid metal is directly deposited. By eliminating the need for powders and high-energy laser systems, MMD offers a potentially more cost-effective and energy-efficient route, particularly suited for lower-melting-point alloys such as Al-Si alloys. Nevertheless, the relationships between processing parameters, layer geometry and microstructure in MMD remain insufficiently understood.

In this study, five 4043 aluminium alloy samples were fabricated by MMD under varying printing speeds, nozzle temperatures and substrate temperatures. The structures were analysed macroscopically and microscopically using optical microscopy and SEM, and quantification of primary α-Al grains and Fe-rich intermetallic compounds (IMCs). Interlayer junction width was sensitive to build height and processing conditions, reflecting the roles of wetting, spreading and prior-layer remelting. In contrast, grain structure and IMC characteristics remained relatively uniform across the processing window. The α-Al grains showed limited columnar features, while local Si enrichment at junctions indicated partial remelting of eutectic regions, enhancing interlayer bonding. Secondary dendrite arm spacing suggested cooling rates of ~10–100 K s^{-1}, sufficient for microstructural refinement despite being lower than in laser-

based AM. Fe-rich IMCs were finely dispersed in interdendritic regions, with median lengths below 4 μm and minimal variation between layers.

Statement on use of generative AI

I declare that my use of generative AI tools complies with applicable University, divisional, and departmental policy and guidance.

Generative AI tools used:

- ChatGPT (GPT5.5, OpenAI) – used to proofread the thesis and improve the clarity, language and style of the writing.
- ChatGPT (GPT5.5, OpenAI) – used for assistance with data analysis on the correlation between IMC size and morphology, and MMD processing conditions, especially real-time nozzle temperature.
- ChatGPT (GPT5.5, OpenAI) – Introduction to Al alloys selected and specifically designed for AM processes and Table 2.3 in section 2.4.

Declaration of Originality

The work described in this thesis was carried out by the author in the Department of Materials, University of Oxford, under the supervision of Prof. Patrick Grant and Dr. Enzo Liotti. This thesis is submitted for the degree of Master by Research at University of Oxford. I hereby declare that all of the work in this thesis is original and my own, except as specified in Acknowledgements or in the text, and that no part of the thesis has been submitted for a degree at this or any other university.

Acknowledgements

I would like to express my gratitude to Prof. Patrick Grant and Dr. Enzo Liotti for offering me the chance to work in the group and guidance in research.

And, I am also grateful to Dr. Shikang Feng and Ruining Jin for training me on experiments and project management.

I would also like to extend my thankfulness to Valcun for manufacturing the materials and trust in my ability on preparing the samples and analyzing the data.

Contents

1 Introduction 12

Aims and Objectives

Thesis structure

Publications

2 Literature review 17

2.1 Overview of additive manufacturing (AM) 17

2.2 Classification of AM processes for metals 18

2.3 Molten Metal Deposition 20

2.4 AM of Aluminium Alloys: Processability, Limitations and Applications 22

2.5 Al AM microstructure 27

Effect of melt-pool shape

Grain morphology and anisotropy

Effect of reheating

Grain refinement

Defects

3 Experimental methods 35

3.1 MMD sample fabrication 35

3.2 Wedge casting 38

3.3 Metallographic preparation 39

3.4 Electron microscopy 39

3.5 Sample geometrical consistency measurement 41

3.6 IMC morphology analysis 41

3.7 Grain size measurement 42

3.8 SDAS measurement 42

4 MMD microstructure of a 4043 Al alloy 44

4.1 Results 45

4.1.1 MMD samples 45

Dimensional consistency

Microstructure

Grain size analysis

IMC size and morphology

4.1.2 Wedge-casting microstructure 58

4.2 Discussion 60

4.2.1 Influence of process parameters on layer geometry 60

4.2.2 Influence of process parameters on the microstructure 61

4.2.3 Comparison with L-PBF and wedge casting 63

7 Conclusions 66

8 Further work 69

9 Bibliography 71

List of figures

Figure 1.1. Fields of applications of Al alloys. 12

Figure 2.1. Schematic illustration of the Laser-Powder Bed Fusion (L-PBF) process and associated multiple physical and chemical phenomena, showing the various phenomena influenced by laser-powder interaction, solidification and solid-state transformation [43]. ..28

Figure 2.2. Macrostructure of SLM (L-PBF) processed Al-Si alloy determined by the way different melt pools are combined, i.e., the building strategy of the components; (a) front view showing the half-cylindrical melt pools overlapping with each other; (b) top view showing the cross section of the melt pools and the discontinuity due to the variation in depth and shape of the melt pools [58]. 28

Figure 2.3. L-PBF processed hypereutectic Al-50Si alloy. The melt pool, primary Si and eutectic Si distribution within it are identified [43]. 30

Figure 2.4. Hypereutectic AlSiMg alloy microstructural feature: EBSD image showing primary-Al columnar grains with a <001> fibre texture in the build direction (ZY), adapted from Kotadia et al. [43]. 31

Figure 2.5. Schematic of the microstructural evolution of PBF-processed samples during annealing. Si-rich areas are represented as red [48]. 32

Figure 2.6. Grain refinement of Al alloys by solute and nucleant particle addition in L-PBF. (a, b) AlSi10Mg with and without TiB2 [64]. (c, d) AlSi10Mg with and without LaB6 [65], [66]. (e, f) 2024 alloy with and without Ti [52]. (g, h) Al-1.5Mg- 0.2Sc-0.1Zr with and without addition of Si and higher Mg [67]. (i-l) Al-Mg-Zr with and without Sc with different energy

densities [68]. (m, n) 7075 alloy with and without ZrH2 [46]. (o, p) 7075 with and without addition of Si [69]. 33

Figure 2.7. The different types of defects that form during AM of Al-Si alloys by L-PBF: (a) balling, (b) gas pores, (c) voids or lack-of-fusion pores and (d) hot cracking [43]. 34

Figure 3.1. Schematic showing the components and procedures of molten metal deposition technique. 35

Figure 3.2. Images of sample R688 (a) full-length sample; (b) Optical micrograph showing the centre and junction widths. 36

Figure 3.3. Printing parameters for the five samples: printing speed, substrate temperature, nominal nozzle temperature, measured nozzle temperature, for each sample as a function of print height. 37

Figure 3.4. Schematic of the half of the wedge mold showing the dimensions (in mm) used in this investigation. 38

Figure 3.5. (a) the wedge-mold with labels of the five areas – tip a, tip b, middle, heel c, and heel d; (b) schematic showing the cooling rates within each region estimated from the SDAS analysis. 39

Figure 3.6. Three regions selected for electron microscopy, representing the morphological characteristics, on sample R748: (a) centre region; (b) junction region; (c) edge region. 40

Figure 3.7. Demonstration of the procedure of image processing (a)(b)(c) image normalization at different Mag; (d)(e) image segmentation using the binary mask of the selected cluster of IMCs. 42

Figure 4.1. (a) junction and centre width of sample R693, R688, R699, R749 and R748; and (b) ratio. 45

Figure 4.2. (a) junction width and (b) centre width plotted as a function of layer number. ... 46

Figure 4.3. SEM images of centre and junction regions at layer22 of sample R693: (a) overview of the layer; (b) centre region; (c) junction region; (d) IMC concentration at the junction where IMCs were identified as phase in white by BSE detector. 47
Figure 4.4. Junction area by secondary electron signal (UHD detector) at layer78 of R748 at different magnification (a): × 300; (b): × 800; (c): × 3k; (d) × 6k. 48
Figure 4.5. SEM images by backscatter electron signal (SBED detector) from bottom, middle, and top layers of each sample junction at 300 Mag (a) column for bottom layer; (b) column for middle layer; (c) column for top layer of the print. 49
Figure 4.6. SEM images by backscatter electron signal (SBED detector) from bottom, middle, and top layers of each sample centre at 300 Mag (a) column for bottom layer; (b) column for middle layer; (c) column for top layer of the print. 50
Figure 4.7. Comparison of grain size of (a) R688 and (b) R748. 51
Figure 4.8. Measurement of grain size of R688 (a) layer1; (b) layer2; (c) layer3; (d) layer4; (e) layer14; (f) layer82; (g) layer83. 52
Figure 4.9. Measurement of grain size of R748 (a) layer1; (b) layer10; (c) layer11; (d) layer76; (e) layer77; (f) layer78. 52
Figure 4.10. (a) SDAS at centre region; (b) SDAS at junction region; (c) cooling rate at centre region; (d) cooling rate at junction region as a function of layer number. 53
Figure 4.11. IMC phase measurements of junction region of all five samples with corresponding nozzle temperatures of each layer (a) overall area; (b) area fraction; (c) aspect ratio; (d) length; (e) width. 55
Figure 4.12. Sample-by-sample variance of IMC area, aspect ratio, length, and width distribution at centre region. Percentile 0.95 (P95) and 0.05 (P05) of IMC measurements of each layer were derived. P95 – mean and mean – P05 were plotted as upper error and lower

error, respectively. (a) column for area; (b) column for aspect ratio; (c) column for length; (d) column for width. 56

Figure 4.13. Sample-by-sample variance of IMC area, aspect ratio, length, and width distribution at junction region. Percentile 0.95 (P95) and 0.05 (P05) of IMC measurements of each layer were derived. P95 – mean and mean – P05 were plotted as upper error and lower error, respectively. (a) column for area (b) column for aspect ratio; (c) column for length; (d) column for width. 57

Figure 4.14. Comparison of IMC measurements of all five samples (a) overall area; (b) area fraction; (c) aspect ratio; (d) length; (e) width. 58

Figure 4.15. SEM images of the wedge-casted 4043 Al alloy showing morphology at five different positions in the wedge with corresponding cooling rate (a) tip a – 86.61 ± 33.10 K/s; (b) tip b – 26.93 ± 7.90 K/s; (c) Middle – 16.20 ± 3.46 K/s; (d) heel c – 11.44 ± 4.91 K/s; (e) heel d – 11.24 ± 4.52 K/s. 59

Figure 4.16. SDAS of 4043 Al alloy made by wedge casting (a) SDAS against positions of the wedge; (b) SDAS against cooling rates. 59

Figure 4.17. IMC measurement against cooling rates (a) IMC area; (b) IMC area fraction; (c) IMC aspect ratio; (d) IMC length; (e) IMC width; (f) IMC number density. 60

Figure 4.18. IMC measurements against positions in the wedge (a) IMC area; (b) IMC area fraction; (c) IMC aspect ratio; (d) IMC length; (e) IMC width; (f) IMC number density. 60

Figure 4.19. Comparison between microstructures of cross-sections produced by MMD and L-PBF (a)(c) as-manufactured 4043 sample by MMD; (b)(d) AlSi10Mg by L-PBF [1], [2]. ... 65

List of tables

Table 2.1 Representative AM equipment sources and specifications [3]. 19

Table 2.2 List of selected Al alloys used in L-PBF [4]. 22

Table 2.3 Al alloys specifically designed for AM. 24

Table 3.1. Printing conditions for each sample. 36

Chapter 1

Introduction

Aluminium alloys are of considerable technological importance in aerospace, automotive, transport and construction applications, where reductions in structural mass can deliver improvements in energy efficiency, fuel economy and overall component performance (Fig 1.1). Their widespread use arises from a favourable combination of low density, good specific strength, corrosion resistance, and formability. In the automotive sector, for example, the substitution of conventional steel structures with aluminium body components can provide substantial weight savings, thereby contributing to reduced fuel consumption and lower emissions [5]. In aerospace applications, high-strength aluminium alloys remain important structural materials because they offer an attractive balance between mechanical performance and weight [6].



Figure 1.1. Fields of applications of Al alloys.

Additive manufacturing (AM) offers new opportunities for the fabrication of aluminium components with complex geometries that cannot readily be produced by conventional manufacturing routes, enabling near-net-shape production, reduced material waste and the creation of intricate internal features through layer-by-layer construction from digital designs. This is particularly attractive for lightweight engineering, where topology-optimised geometries, thin-walled structures and lattice architectures can improve structural efficiency, making AM an important area of research for aluminium alloy components in sectors where mass reduction, design flexibility and efficient material use are critical [7].

However, the additive manufacturing of aluminium alloys remains associated with significant scientific and technological challenges, particularly in powder-bed processes where high laser reflectivity, high thermal conductivity, oxide formation and poor powder flowability can lead to unstable melt-pool behaviour, porosity and lack-of-fusion defects. In addition, the use of fine aluminium powders introduces safety concerns related to reactivity, combustibility and inhalation risks [8], [9], while steep thermal gradients and rapid solidification can promote residual stresses, microstructural anisotropy and cracking, thereby motivating the development of alternative AM routes that improve process stability, safety and cost-effectiveness while retaining design flexibility.

Molten Metal Deposition (MMD) is a comparatively recent wire-fed additive manufacturing process in which metallic feedstock is melted within a heated nozzle and deposited directly in the liquid state onto a substrate or previously deposited layer, thereby eliminating the need for a powder bed and reducing reliance on high-power lasers. The use of wire feedstock offers advantages in terms of safety, material utilisation, cost and process simplicity, while independent control of nozzle and substrate temperatures enables adjustment of thermal conditions during deposition, which is particularly important for aluminium alloys due to their sensitivity to heat input and cooling rate [8], [9], [10]. However, despite these advantages, the

process–structure relationships in MMD remain insufficiently understood. Compared with more established techniques such as laser powder-bed fusion and directed energy deposition, liquid-fed MMD has received limited attention, and the effects of key parameters such as nozzle temperature, substrate temperature and printing speed on layer geometry, α-Al grain morphology and secondary intermetallic compound formation have yet to be systematically established [10], [11], [12]

Aims and Objectives

This thesis addresses this knowledge gap by examining 4043 aluminium alloy samples manufactured by Molten Metal Deposition under different combinations of printing speed, nozzle temperature and substrate temperature. The work combines macroscopic examination of layer morphology with microstructural characterisation of the deposited material. Particular attention is given to interlayer junctions, since these regions are expected to play an important role in bonding between successive layers and may be sensitive to local remelting and heat accumulation during the build. The primary α-Al grain structure and the distribution of Fe-rich intermetallic compound particles are also examined in order to assess the extent to which MMD processing conditions influence microstructural development. The specific objectives are to:

1. Characterise the macroscopic morphology and layer geometry of MMD-manufactured 4043 aluminium alloy samples produced under different processing conditions.
2. Assess the influence of printing speed, nozzle temperature and substrate temperature on interlayer junction formation, spreading and remelting behaviour.
3. Examine the primary α-Al grain structure across different regions of the deposited samples and determine the extent of microstructural variation with build height and processing condition.

4. Quantify the size, morphology and distribution of secondary Fe-rich intermetallic compound particles, and evaluate their sensitivity to the thermal conditions generated during MMD.
5. Relate the observed microstructures to estimated cooling conditions, including comparison with wedge-cast samples solidified under different cooling rates.
6. Establish process–structure relationships that can support future optimisation of MMD processing conditions for aluminium alloy additive manufacturing.

The thesis seeks to clarify the mechanisms governing microstructure formation in MMD-processed 4043 aluminium alloy. More broadly, the work evaluates the potential of Molten Metal Deposition as a safer and more flexible alternative to powder-based aluminium additive manufacturing, particularly for applications requiring controlled layer geometry, refined microstructure and reliable interlayer bonding.

Thesis structure

This thesis is organized as follows:

Chapter 2 reviews the relevant literature on additive manufacturing of metals, specifically powder bed processes. It also covers the aluminium alloys used for AM and the micrsostructure typically obtained.

Chapter 3 describes the methodologies employed to fabricate and investigate the materials.

Chapter 4 presents the results of the macroscopic layer-geometry analysis and microstructural characterisation. The findings are discussed in relation to the selected processing parameters and contextualised within the AM literature on 4043 aluminium alloy.

Chapter 5 contains the conclusions of the work.

Chapter 6 suggests possible future work.

Publications

The results of the analysis have been summarised in the following journal publication:

- M. Dai, S. Feng, J. Galle, C. Elangeswaran, P. S. Grant, and E. Liotti, Molten metal deposition of 4043 Al alloy towards more uniform dendritic microstructure and refined Fe-rich intermetallics, *Additive Manufacturing,* in preparation.

Chapter 2

Literature review

2.1 Overview of additive manufacturing (AM)

The manufacturing routes of metals can be categorized into formative manufacturing, subtractive manufacturing, and additive manufacturing. Formative manufacturing processes include casting, forging, and welding, while subtractive manufacturing processes include turning, milling, and grinding. Additive manufacturing (AM) can be referred to as three-dimensional (3D) printing and construct complex-shaped components in a layer-by-layer deposition process [11], [13]. AM is considered a useful method to produce high-performance near-net shape components due to its fabrication advantages, *i.e.,* short production time and almost no material waste [14]. It enables distributed manufacturing and the productions of parts-on-demand while offering the potential to reduce cost, energy consumption, and carbon footprint [3]. Initially developed in mid 1980s, AM started as a rapid prototyping and concept models in plastics and is considered as a polymer-based technology [15]. As one of the earlier AM processes, rapid prototyping presented advantages of time and cost reduction, human interaction, and consequently the production development cycle [16], as well as the modelling of parts with shapes difficult for machining [17]. The term additive manufacturing was defined in an ASTM standard in 2009 [18] as: "a process of joining materials to make objects from 3D model data, usually layer upon layer, as opposed to subtractive manufacturing methodologies. Synonyms: additive fabrication, additive processes, additive techniques, additive layer manufacturing, layer manufacturing, and freeform fabrication." This definition could be extensively applied to all classes of materials, *i.e.,* metals, ceramics, polymers, composites, and

biological systems [3]. Advances in CAD and high powder-bed lasers has also enabled AM processes to enter the metal realm. With new manufacturing processes, new alloys employed for AM, and new applications in aerospace, medical, automotive and energy, AM has been considered as one of the most dynamic frontiers in modern manufacturing research [15].

2.2 Classification of AM processes for metals

AM procedure can be regarded as a multiple-welding process. The methods of classifying AM systems are based on the material feedstock, energy source, build volume [3]. They can be further divided in melt-based AM and solid-state-based AM, depending on layer bonding method and consolidation mechanism [3][4].

Melt-based AM melt and solidify the feedstock materials with the heat sources provided either by a laser beam, an electron beam, or an arc. The melt-based AM processes include powder bed fusion and direct energy deposition. Powder bed fusion consists of L-PBF (laser powder bed fusion) and EB-PBF (electron beam powder bed fusion) [20]. Direct energy deposition consists of EBFF (electron beam freeform fabrication), WLAM (wire laser additive manufacturing), LP-DED (laser powder direct energy deposition), and WAAM (wire-arc additive manufacturing) techniques [4][5].

Solid-state-based AM joins the adjacent layers through sintering or mechanical bonding. The solid state-based AM processes include sinter-based AM and mechanical-deformation-based AM. Sinter-based AM provides the driving force for material bonding through thermal bonding (sintering) and it consists of BJ (binder jetting) [22], ME (metal extrusion) [23], and SP (screen or stencil print) [24]. Mechanical-deformation-based AM facilitates layer bonding by employing kinetic energy and it can be divided into UAM (ultrasonic additive manufacturing) [25], AFSD (additive friction stir deposition) [26], and CS (cold spray) [27] depending on kinetic energy delivery method. A short introduction of UAM procedure is given here to

illustrate the fundamental mechanism of Mechanical-deformation-based AM: as a solid-state welding process, UAM utilizes ultrasonic energy to build complex three-dimensional components from metal foil. A thin metal tape is initially bonded ultrasonically to a substrate material, with additional tapes being subsequently bonded to the previous layer. Computer controlled milling operations are incorporated to create intricate internal cooling channels during processing and maintain complex part geometries.

AM systems could also be divided, according to the feeding mechanism, into three classes: (1) powder bed; (2) powder feed; (3) wire feed systems. Table 2.1 is a summary of commercially available systems with the corresponding energy sources including electron beam, laser and arc [3].

Table 2.1 Representative AM equipment sources and specifications [3].

System	Process	Building volume (mm^3)	Energy source
Powder bed			
ARCAM (A2)(a)	EBM	200 × 200 × 350	7 kW electron beam
EOS (M280)(b)	DMLS	250 × 250 × 325	200-400 W Yb-fibre laser
Concept laser cusing (M3)(b)	SLM	300 × 350 × 300	200 W fibre laser
MTT (SLM 250)(b)	SLM	250 × 250 × 300	100-400 W Yb-fibre laser
Phenix system group (PXL)(c)	SLM	250 × 250 × 300	500 W fibre laser
Renishaw (AM 250)(d)	SLM	245 × 245 × 360	200 or 400 W laser
Realizer (SLM 250)(b)	SLM	250 × 250 × 220	100, 200, or 400 W laser

Matsuura (Lumex Advanced 25)(e)	SLM	250 × 250 diameter	00 W Yb fibre laser; hybrid additive/subtractive system
Powder feed			
Optomec (LENS 850-R)(f)	LENS	900 × 1500 × 900	1 or 2 kW IPG fibre laser
POM DMD (66R)(f)	DMD	3,200° × 3°, 670° × 360°	1-5 kW fibre diode or disk laser
Accufusion laser consolidation(g)	LC	1,000 × 1,000 × 1,000	Nd: YAG laser
Irepa laser (LF 6000)(c)	LD		Laser cladding
Trumpf(b)	LD	600 × 1,000 long	
Huffman (HC-205)(f)	LD		CO2 laser clading
Wire feed			
Sciaky (NG1) EBFFF(f)	EBDM	762 × 483 × 508	>40 kW @ 60 kV welder
MER plasma transferred arc selected FFF(f)	PTAS FFF	610 × 610 × 5,182	Plasma transferred arc using two 350A DC power supplies
Honeywell ion fusion formation(f)	IFF		Plasma arc-based welding
Country of Manufacturer: (a) Sweden, (b) Germany, (c) France, (d) United Kingdom, (e) Japan, (f) United States, and (g) Canada			

2.3 Molten Metal Deposition

Molten metal deposition (MMD) is a wire-fed process in which Al is melted in a crucible and deposited in a liquid form. The process offers several potential advantages over powder-bed AM routes. The use of wire feedstock eliminates the risk of explosion, oxidation or inhalation hazards. The higher deposition rate also reduces the feedstock cost, in turn decrease part fabrication time and overall implementation cost [28]. It also avoid issues like powder flowability, spreading defects, moisture absorption, and powder bed density variation, thereby producing a more homogeneous microstructure [29] [30]. Additionally, no support material is required for the manufacturing of components with complex geometries [8].

MMD, as developed by ValCUN (Belgium), was utilized by Kapil et al. [31] to address challenges commonly encountered in the AM of aluminium alloys including porosity, low mechanical properties, and solidification shrinkage. The continuous extrusion of molten metal enables relatively high build rates and adaptive resolution, making the process suitable for medium-sized components with complex geometries. To improve control over process parameters and dimensional accuracy, they investigated the post-impingement behaviour of molten aluminium droplets and analysed the resulting deposit geometry. Their work provided insight into how the initial conditions of molten droplets influence spreading, solidification and final feature shape during MMD.

The influence of process parameters on the thermal behaviour, porosity, and mechanical properties of 4043 aluminium alloy structures was investigated by Hoekstra et al. [32]. Layer-wise deposition was simulated using a conduction-based thermal model, which was validated against in situ thermocouple measurements at various build heights. The study demonstrated the viability of MMD for producing 4043 wall structures with low porosity and favourable strength–ductility combinations, while also providing a model-driven framework for parameter optimisation in melt-pool-free deposition. It was shown that substrate temperature, nozzle

temperature, and travel speed play significant roles in controlling porosity, surface waviness and deposition efficiency.

Menapace et al. [8] fabricated three types of samples from two Al alloys (4043 and 6061) using the MMD technique. The defects, density, and microstructure of the resulting components were evaluated, and microhardness measurements were conducted. The results indicated that, with appropriate process parameters, a fine microstructure can be achieved, leading to improved mechanical performance.

Whereas, several disadvantages arise due to the intrinsic properties result from MMD process itself. The first is the relatively lower cooling rate of MMD, comparing with other AM processes, especially PBF which stands out for its refined microstructure because of its high cooling rate. The second is the fragility of the interlayer junction region. The junction width is controlled by the local remelting and wetting, and the precipitation of IMCs and Al-Si eutectic reaction at junction are repeated in heat treatment via thermal cycles. For the geometry of the lower width, as well as concentration of eutectic phase and IMCs, the junctions could be a potentially fracture region of MMD-processed components in the service as a structural material.

2.4 AM of Aluminium Alloys: Processability, Limitations and Applications

Despite being among the earliest metallic materials investigated for additive manufacturing (AM), aluminium alloys have been relatively slow to achieve widespread adoption in powder-bed fusion (PBF) processes [19], [29], [33], [34]. This is largely due to several intrinsic characteristics of aluminium alloys that complicate melt-based processing, including high thermal conductivity, high solidification shrinkage, broad solidification temperature ranges and, in some alloy systems, poor weldability. These factors can promote unstable melt-pool behaviour, residual stresses, porosity and solidification cracking during AM [35].

The aluminium alloys most successfully processed by AM are typically those with compositions close to the Al-Si eutectic. Silicon improves fluidity, reduces solidification shrinkage and lowers hot-cracking susceptibility, making 4xxx series Al-Si alloys among the most commonly used aluminium alloys for AM [35]–[42]. Al-Si-Mg alloys are also widely used, particularly in as-deposited or heat-treated conditions, because they combine good processability with useful mechanical properties [36], [37]. By contrast, many high-strength heat-treatable aluminium alloys are more difficult to process directly using fusion-based AM due to their susceptibility to hot cracking. For this reason, AM-specific alloy design has focused on improving processability through grain refinement, enhanced heterogeneous nucleation and reduced cracking tendency. Commercially available and specifically designed aluminium alloys for AM are summarised in Tables 2.2 and 2.3.

Table 2.2 List of selected Al alloys used in L-PBF [4].

	Composition	Conditions	Ref.
Cast Alloys	A356 (Al-7Si-0.6Mg)	L-PBF	[38]
		T2	[38]
	AlSi12 (Al-10Si-0.32Mg-0.03Cu)	L-PBF	[33], [39], [40]
		L-PBF + T6	[33], [39], [40]
	AlSi12 (Al-12Si-Fe)	L-PBF	[41], [42], [43]
		L-PBF + Solution heat treatment	[41], [42], [43]
	Al-20Si	L-PBF	[44]
		L-PBF + 400 ◦C for 6 h	[44]
Wrought Alloys	2xxx (2024: Al-4.35Cu-1.50Mg-0.25Fe-	L-PBF with Grain refiner + T6	[45]

	0.60Mn0.08Ti-0.05Cr)		
	2xxx (A20X: Al-4.5Cu-0.3Mg-0.7Ag-3.5Ti)	L-PBF + 530 ◦C for 1 h + 160 ◦C 3 h	[46]
	4xxx (4043: Al-4.5Si-0.8Fe-0.3Cu-0.05Mn-0.05Mg)	Laser Aided Direct Metal Deposition (DMD) / MMD	[8], [47]
	5xxx (Scalmalloy®: Al-4.5Mg-0.6Sc-0.5Mn-0.3 Zr)	L-PBF	[48]
		L-PBF + Aging at 300 ◦C, 5 h	[48]
	6xxx (6061: Al-0.9Mg-0.7Si-0.3Cu-0.3Fe-0.1Ti)	L-PBF (with heated build plate at 500 ◦C)	[49]
	7xxx (7075: Al-5.5Zn-2.5Mg-1.6Cu-0.4Si-0.3Fe0.2Cu-0.2Ti)	L-PBF with Grain refiner + T6	[33]
		L-PBF + T6	[50]
	7xxx (Al-7A77: Al-5.5Zn-1.5Cu-2.5Mg-1.5Zr)		

Table 2.3 Al alloys specifically designed for AM.

Alloy	Developer	Composition Concept
Scalmalloy®	APWORKS (Airbus)	Al-Mg-Sc-Zr
Aheadd® CP1	Constellium	Al-Fe-Zr based

Alloy	Developer	Composition Concept
Aheadd® HT1	Constellium	High-temperature Al alloy
M789-Al variants	Various developers	Tailored precipitation-strengthening alloys
Addalloy® 5T	Equispheres	High-strength crack-resistant alloy
Al-Mg-Sc-Zr alloys	Various research groups	Grain-refined AM alloys
Al-Ce-Mg alloys	HRL Laboratories / Eck Industries	Excellent castability and AM printability
NASA Al-Ce-X alloys	NASA / HRL	Designed for high-temperature AM applications

The limited adoption of aluminium alloys in AM is also partly related to the maturity of conventional processing routes. Aluminium alloys can already be cast into complex shapes and processed by wrought routes due to their good castability and formability [51]. Therefore, AM must offer clear advantages in design freedom, material efficiency, performance or lead time to justify its use. In PBF, however, several powder-related and laser-material interaction challenges remain. Aluminium powders are highly reflective to laser radiation, meaning that a significant fraction of the incident energy may be reflected rather than absorbed. As a result, higher energy input and more careful parameter control are often required to achieve stable melting. The high thermal conductivity of aluminium further promotes rapid heat dissipation, making it difficult to maintain a stable melt pool and increasing the risk of lack-of-fusion defects. A further challenge is the presence of a thin but stable aluminium oxide layer on powder surfaces. Aluminium oxide has a much higher melting point than aluminium itself and can inhibit metallurgical bonding if it is not disrupted during processing [29]. This oxide film can contribute to porosity, cracking and weak interlayer bonding. Aluminium powders may

also exhibit poor spreadability, leading to uneven powder layers, local variations in packing density and defects in the final part. Moisture absorption by powder feedstocks can introduce additional problems during melt-based processing, including hydrogen-related porosity [29], [52]. Together, these issues make powder handling, storage and processing particularly important for aluminium AM.

The processability of aluminium alloys also depends strongly on the AM route. In sintering-based solid-state AM, a carefully controlled atmosphere with low oxygen and vapour partial pressure may be required to limit oxidation and promote atomic diffusion during sintering. This increases process complexity and cost [53]. By contrast, deformation-based solid-state AM processes are often more suitable for aluminium alloys because they exploit the high ductility and formability of aluminium rather than relying on complete melting [53]. These approaches can reduce problems associated with solidification cracking and oxide-related defects, although they may impose other limitations in terms of geometry, resolution and surface finish.

Beyond material-specific issues, metal AM more generally faces challenges associated with build speed, support structures, surface quality and property reliability [18]. The production of large metallic components can require long build times, sometimes extending over several days, which increases cost and limits productivity. Although high-rate processes such as cold spray AM have been adapted for metallic materials, there remains a need for faster manufacturing routes capable of producing high-quality metal components with reliable properties [18]. Support structures represent another important limitation in many metal AM processes. They are commonly required to anchor the part to the build plate, reduce distortion and support overhanging features during printing. However, support structures increase material use, extend build time and require additional post-processing for removal. In some cases, components may distort or detach from the substrate during fabrication, particularly when residual stresses are high. Surface finish is also a persistent challenge in metal AM, and

extensive post-processing may be required to meet dimensional and surface-quality requirements. Hybrid systems that combine additive and subtractive manufacturing have therefore been developed to improve surface finish and dimensional accuracy [18].

Finally, the consistency and reliability of AM components remain critical barriers to wider industrial application. Geometrical imperfections, porosity, residual stresses, microstructural anisotropy and surface roughness can all reduce fatigue resistance, fracture toughness and overall mechanical performance. These issues are particularly important for safety-critical applications in aerospace, automotive and energy systems, where components must meet strict performance and qualification requirements. Although multi-material AM offers opportunities for embedded electronics, local microstructural control and functionally graded structures, it also introduces additional challenges associated with material compatibility, interfacial bonding and process control [18]. Addressing these limitations is therefore essential for the broader adoption of aluminium alloys in additive manufacturing.

2.5 Al AM microstructure

The microstructure of aluminium alloy components produced by additive manufacturing is primarily governed by the morphology and thermal history of the melt pool generated by the moving heat source. Although melt-pool characteristics, such as size, aspect ratio and penetration depth, vary with the AM process and processing parameters, including laser or electron-beam power, scan speed and hatch spacing, they share several common features [12]. These include rapid melting, directional heat extraction, high cooling rates, local solute redistribution, fluid flow and repeated thermal cycling. Together, these phenomena give rise to the distinctive microstructural features that develop as successive tracks and layers are deposited.

Effect of melt-pool shape

Components fabricated by powder bed fusion (PBF) consist of overlapping melt pools formed by the melting of powder using a moving heat source (Fig 2.1). A characteristic feature of additively manufactured Al-Si alloys is the formation of fine cellular or dendritic α-Al structures, together with a refined eutectic Si network. However, grain morphology should not be generalised into a fixed centre-to-boundary pattern for every melt pool. In hypoeutectic Al-Si alloys processed by L-PBF, primary α-Al commonly grows epitaxially from the partially remelted layer below, producing columnar or cellular grains that can extend through successive layers and are often aligned with the build direction [4]. Equiaxed grains may form under particular alloy chemistries, nucleant additions, or solidification conditions that promote a columnar-to-equiaxed transition, but this is not the default morphology for every melt pool. The overlap, curvature and depth variation of melt pools, as illustrated in Fig 2.2 for Al-Si alloys produced by selective laser melting (SLM), are therefore defining structural features of PBF-fabricated materials and contribute to microstructural anisotropy.

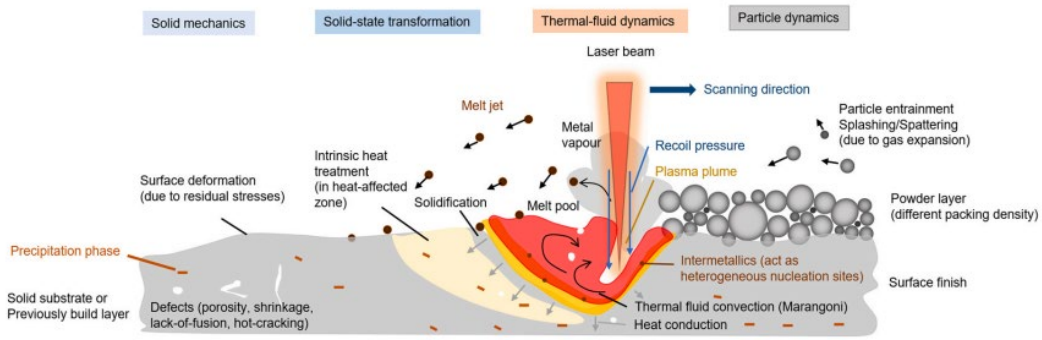


Figure 2.1. Schematic illustration of the Laser-Powder Bed Fusion (L-PBF) process and associated multiple physical and chemical phenomena, showing the various phenomena influenced by laser-powder interaction, solidification and solid-state transformation [43].

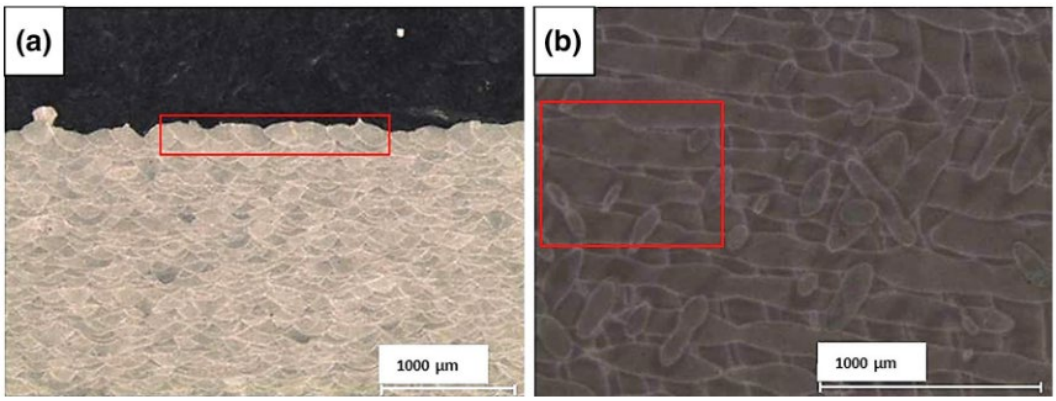


Figure 2.2. Macrostructure of SLM (L-PBF) processed Al-Si alloy determined by the way different melt pools are combined, i.e., the building strategy of the components; (a) front view showing the half-cylindrical melt pools overlapping with each other; (b) top view showing the cross section of the melt pools and the discontinuity due to the variation in depth and shape of the melt pools [58].

Because the heat source moves continuously, the temperature gradient, interface growth rate, cooling rate and melt-flow conditions vary across each melt pool [2], [4]. The curved melt-pool boundary is generally cooler and is connected to partially remelted material from previous tracks or layers, whereas the melt-pool interior remains hotter for longer and may solidify under different local conditions. Marangoni convection, track overlap and partial remelting therefore make the microstructure heterogeneous even over distances comparable to a single melt pool.

The thermal history also differs strongly between PBF and molten metal deposition (MMD). PBF typically involves much higher cooling rates, producing finer microstructures and promoting solute trapping or metastable phases such as Al_6Fe in Al-Fe systems and Al_6Mn in Al-Mn systems [4], [54]. MMD operates at lower thermal gradients, on the order of 10^5 K m^{-1}, and moderate cooling rates below 10^2 K s^{-1}, which can reduce porosity but produces coarser, more slowly solidified structures [32]. Even in PBF, segregation is not eliminated: local microsegregation at cell or grain boundaries and solute enrichment during repeated remelting can still occur, particularly in crack-sensitive high-strength Al alloys [4].

The 4043 Aluminium alloy, containing approximately 5 wt% Si along with minor alloying elements, is a hypoeutectic Al-Si alloy which has a lower Si composition than 12.2 wt% Si of eutectic point on Al-Si phase diagram shown in Fig 2.3. In such alloys, the microstructure produced by PBF typically consists of primary α-Al grains and a secondary eutectic Si phase.

The thermal gradient promotes epitaxial grain growth along preferred crystallographic orientations rather than widespread nucleation within the liquid. This leads to the formation of elongated columnar or cellular grains that can extend across multiple deposited layers and are often aligned with the build direction. The boundaries between these grains are enriched with eutectic liquid, and the morphology of the eutectic Si phase is influenced by factors such as solidification kinetics, thermodynamics and local solute concentration [4].

For hypereutectic Al-Si alloys with Si composition larger than the 12.2 wt% Si of eutectic point, the microstructure includes primary Si particles together with eutectic Si, rather than primary Si being generally described as needles or plates [4]. In conventional casting, primary Si is often faceted or blocky and can be tens of micrometres in size, whereas L-PBF can refine primary Si to sub-micrometre dimensions because of the high cooling rate. Fig 2.4 shows an example of an L-PBF processed hypereutectic Al-50Si alloy in which the melt pool, primary Si and eutectic Si are identified. The high cooling rates associated with PBF can alter the expected phase distribution, such that hypereutectic alloys may exhibit microstructures resembling those of hypoeutectic or eutectic compositions [43]. Regions closer to the heat source or within the melt-pool interior may solidify more slowly and with different solute distributions, while the cooler melt-pool boundaries promote finer primary Si particles and enhanced micro-segregation. The primary distinction between hypoeutectic and hypereutectic Al-Si alloys produced by PBF therefore lies in the relative phase fractions and the nature of primary phase solidification [4].

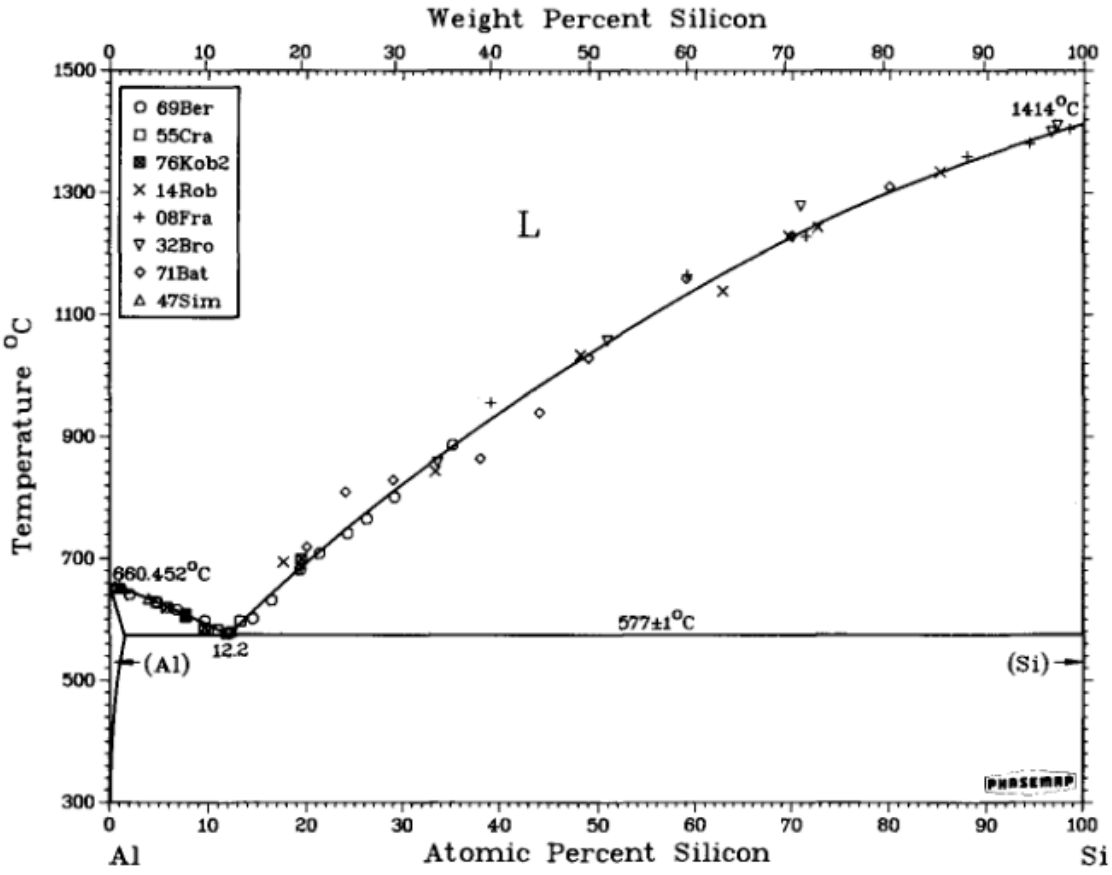


Fig 2.3. Assessed Al-Si phase diagram with selected liquidus data [55].

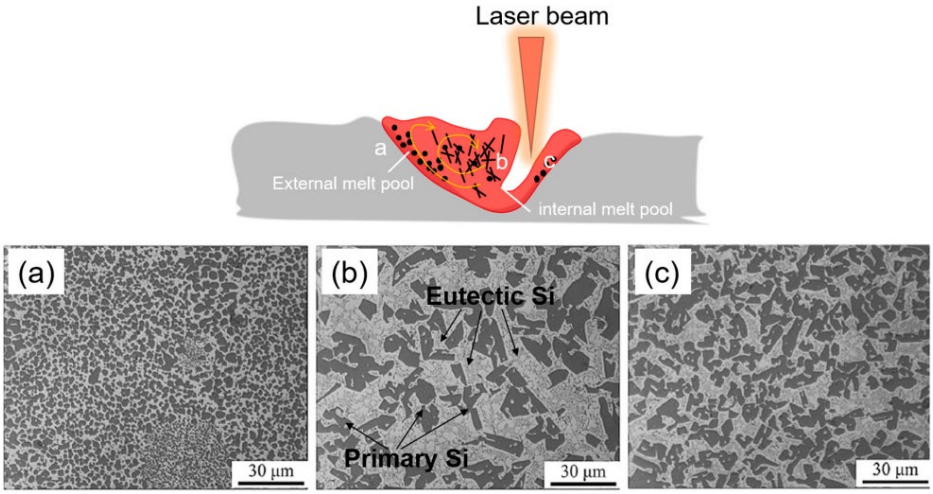


Figure 2.4. L-PBF processed hypereutectic Al-50Si alloy. The melt pool, primary Si and eutectic Si distribution within it are identified [4].

Grain morphology and anisotropy

The thermal gradient between fusion zone and heat-affected zone of PBF-processed sample originates from the localized heat input of heat source at melt pool and heat extraction into the

surrounding material. The steep thermal gradient suppresses the nucleation of new grains ahead of the solidification front and instead promotes the competitive growth of existing grains. As a result, grains tend to elongate along the direction of heat extraction, leading to the formation of columnar microstructures that are characteristic of L-PBF processes. The strong directional heat flow and high thermal gradients therefore drive anisotropic grain growth, producing elongated grains aligned with the build direction, as illustrated in Fig 2.5. Though such columnar grains in the map show a varying crystallographic directions, the majority are aligned parallel to the build direction which is vertical to the substrate [4]. This microstructural anisotropy can give rise to direction-dependent mechanical properties, with variations in strength, ductility and fatigue resistance between the build and transverse directions. Rapid solidification further reduces elemental partitioning and extends solid solubility, which may result in the formation of metastable phases in supersaturated solid solutions and often leads to strengths that exceed those of conventionally cast alloys [56], [57], [58].

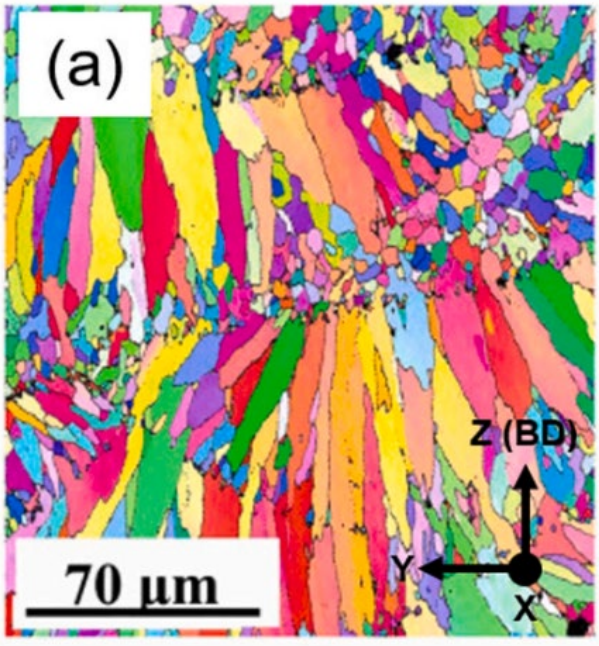


Figure 2.5. Hypereutectic AlSiMg alloy microstructural feature: EBSD image showing primary-Al columnar grains with a <001> fibre texture in the build direction (ZY), adapted from Kotadia et al. [4].

Effect of reheating

During L-PBF, the material is not exposed to a single thermal cycle. Each scan track and subsequent layer partially remelts or reheats the material below, so the final microstructure reflects both the initial rapid solidification event and later thermal exposure. Reheating can relax supersaturation, promote precipitation or other solid-state transformations when the local dwell time and temperature are sufficient, and coarsen features formed during the first solidification step. In Al-Si alloys, this behaviour is related to the annealing evolution of the Si-rich network: fine eutectic Si produced by rapid solidification can spheroidise, coarsen and decrease in number density as thermal exposure increases [4], [41].

This reheating effect can be beneficial or detrimental depending on alloy chemistry and thermal history. Moderate thermal exposure may relieve residual stress or modify precipitates, but repeated remelting and resolidification can also enrich solute at high-angle grain boundaries in crack-sensitive wrought Al alloys, increasing susceptibility to grain-boundary hot cracking [4]. Fig 2.6 should therefore be read as a heat-treatment analogue for the microstructural changes encouraged by repeated AM thermal cycling, rather than as direct proof of the temperature history during every laser pass. Al-12Si produced by SLM show a microstructure with supersaturated Al along with Si-rich region, which is marked as red features, in the cellular boundaries. At low annealing temperature, Si is rejected from primary Al and forming small Si particles. With increasing annealing temperature, the continuing Si enrichment in the boundary promotes Si particle growth. The small Si particles in the track cores surrounded by the larger Si particles in hatch overlaps reinforced the final microstructure.

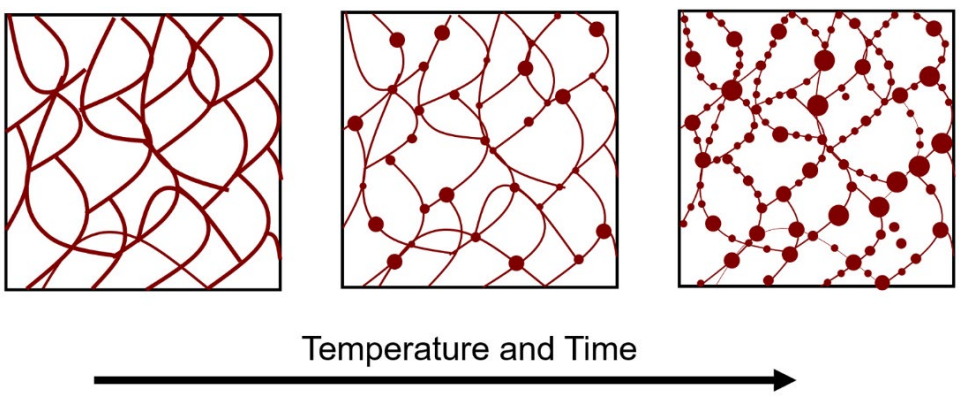


Figure 2.6. Schematic of the microstructural evolution of SLM-processed samples during annealing. Si-rich areas are represented as red [41].

Grain refinement

Grain refinement, achieved through the addition of potent nucleant particles or solute elements, as well as modification of alloy chemistry with silicon, has been identified as an effective approach to mitigate columnar growth, reduce hot-cracking susceptibility and improve processability. Fig 2.7 compiles literature examples reviewed by Kotadia et al. [4]. The examples illustrate significant grain refinement resulting from additions such as TiB_2, LaB_6, Ti, Sc, Zr, ZrH_2 and Si across various alloy systems. These additions can promote heterogeneous nucleation of primary aluminium, increase constitutional supercooling, facilitate the columnar-to-equiaxed transition and break up coarse columnar grains into fine equiaxed structures. Such refinement can reduce microstructural anisotropy, limit crack propagation and improve overall processability. However, excessive additions of intermetallic-forming elements or particles may adversely affect ductility and lead to chemical inhomogeneity.

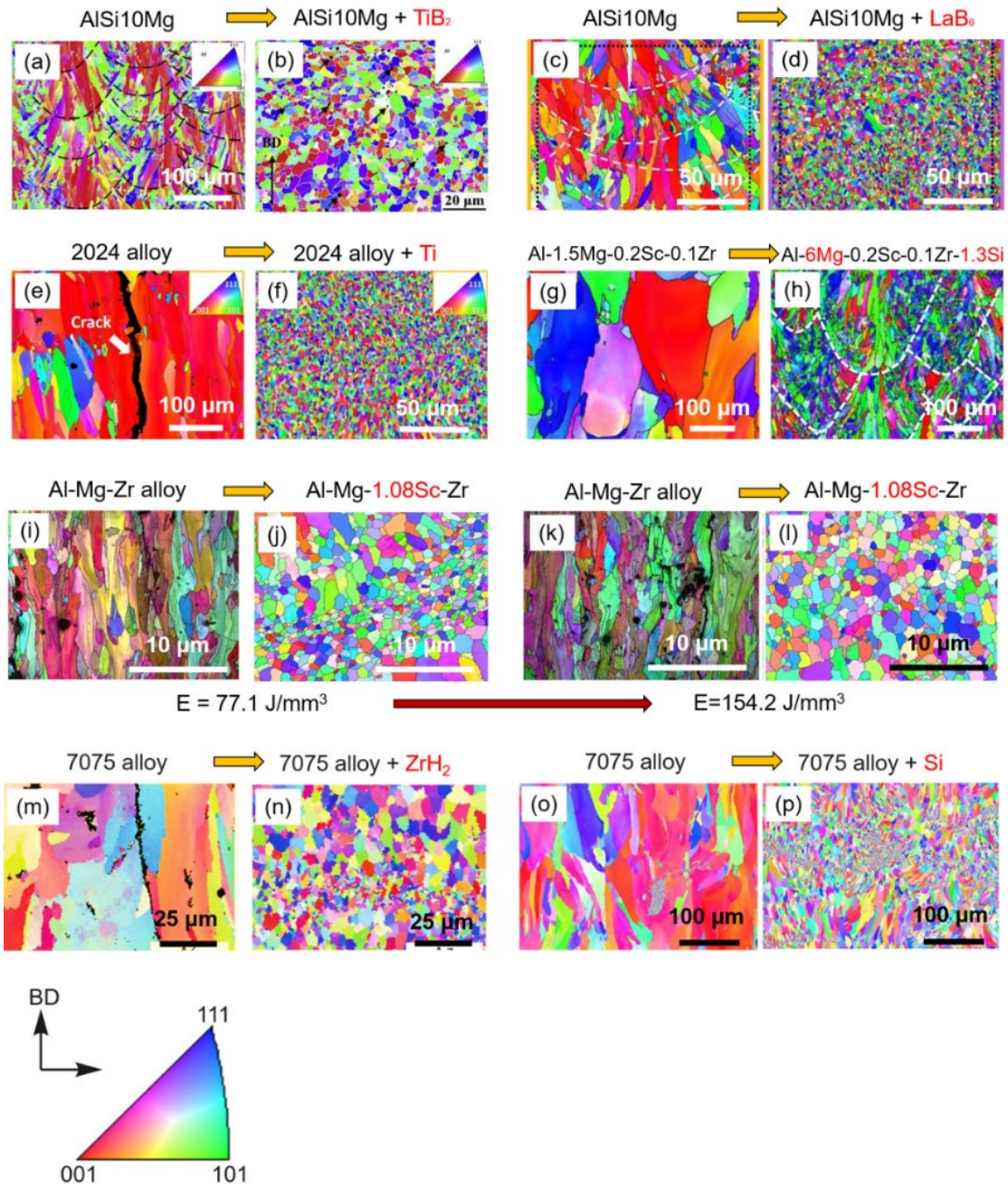


Figure 2.7. Grain refinement of Al alloys by solute and nucleant particle addition in L-PBF. (a, b) AlSi10Mg with and without TiB2 [59]. (c, d) AlSi10Mg with and without LaB6 [60], [61]. (e, f) 2024 alloy with and without Ti [45]. (g, h) Al-1.5Mg- 0.2Sc-0.1Zr with and without addition of Si and higher Mg [62]. (i-l) Al-Mg-Zr with and without Sc with different energy densities [63]. (m, n) 7075 alloy with and without ZrH2 [33]. (o, p) 7075 with and without addition of Si [64].

Defects

Fig 2.8 shows the most common defects in Al-Si alloys processed by L-PBF, including balling, gas porosity, lack-of-fusion pores and hot cracking [4]. Balling is associated with melt-track

instability and poor wetting, producing irregular scan tracks and weak inter-line bonding. Gas porosity can arise from hydrogen introduced by moisture in the powder or from keyhole-mode melting at excessive energy density. Lack-of-fusion pores are typically linked to insufficient energy input, poor overlap between tracks or layers, or unmelted powder regions. Hot cracking occurs when solidification shrinkage, residual stress, grain-boundary segregation and alloy crack sensitivity combine during the final stages of solidification.

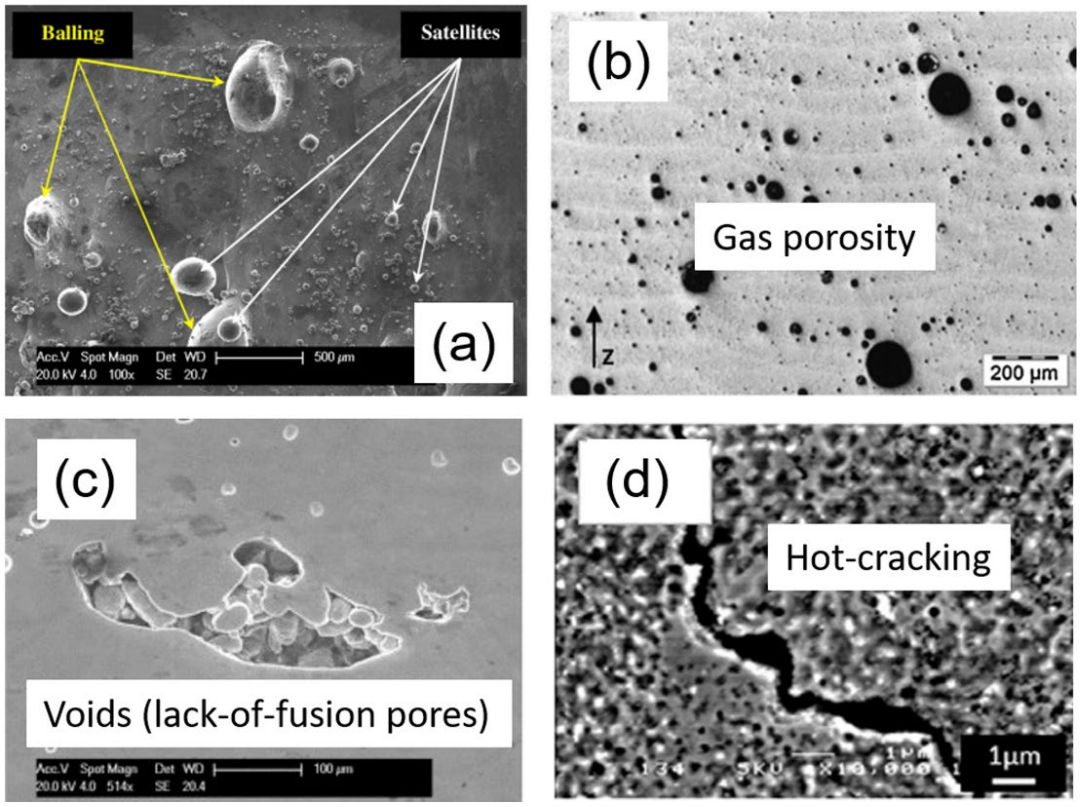


Figure 2.8. The different types of defects that form during AM of Al-Si alloys by L-PBF: (a) balling, (b) gas pores, (c) voids or lack-of-fusion pores and (d) hot cracking [4].

2.5 Research gap

1. As MMD is an innovative alternative method to PBF, there are few literatures illustrating difference between the microstructure produced by MMD and PBF. In this work, microstructure of five MMD-processed samples fabricated using different processing parameters was firstly characterized using SEM and then compared with that of PBF.

2. Influence of processing parameters on sample geometry is vitally important because the MMD-processed samples have a layer-by-layer geometry which requires great attention for improving mechanical performance. Junction width, centre width, and junction / centre width ratio of the five samples were measured using Optical microscopy and plotted against layer numbers. The decrease in junction width of R748 and R688, and consistency of centre width indicate the geometrical change at different printing conditions.

3. Influence of processing parameters on microstructural evolution needs to be studied. The potential role of cooling rate on effecting size, morphology, and distribution of Fe-rich IMCs during MMD processing with different parameter design also needs to be investigated to optimize material design. In this work, area, area fraction, aspect ratio, length, and width of IMCs were measured using Bespoke Matlab script after segmentation and plotted against layer number. Sample-by-sample variance of IMC measurements were also analyzed to investigate the microstructural change at different processing conditions.

4. One of the main advantages of MMD is its welding-like AM process which produces more refined microstructure than that of casting process and less columnar structure than that of PBF process. No literature has given a direct comparison of microstructure between MMD and casting processes. This project includes the microstructure characterization and IMC measurements of a wedge-casted sample, as well as measurements on SDAS and derivation of cooling rates at different regions. The microstructure change was compared with that of MMD samples to validate the role of cooling rate on controlling size, morphology, and distribution of Fe-rich IMCs.

Chapter 3

Experimental procedure

3.1 MMD sample fabrication

Work primarily focused on the investigation of samples produced with a new molten metal additive manufacturing technology developed by our industrial collaborator Valcun (Belgium) [31] [65] [32] [8]. Fig 3.1 is a schematic of the molten metal deposition technique. In this process, an Al wire is fed to a heating chamber and melted. The liquid metal is then deposited through a nozzle at the bottom, which is heated to between 525 and 970 °C (measured with a thermocouple inserted 5 mm inside the wall of the ceramic chamber). The metal is deposited onto a rotating heated bed. Thus, the ceramic nozzle provided X-Y motion while the build plate rotated, enabling multi-axis deposition.

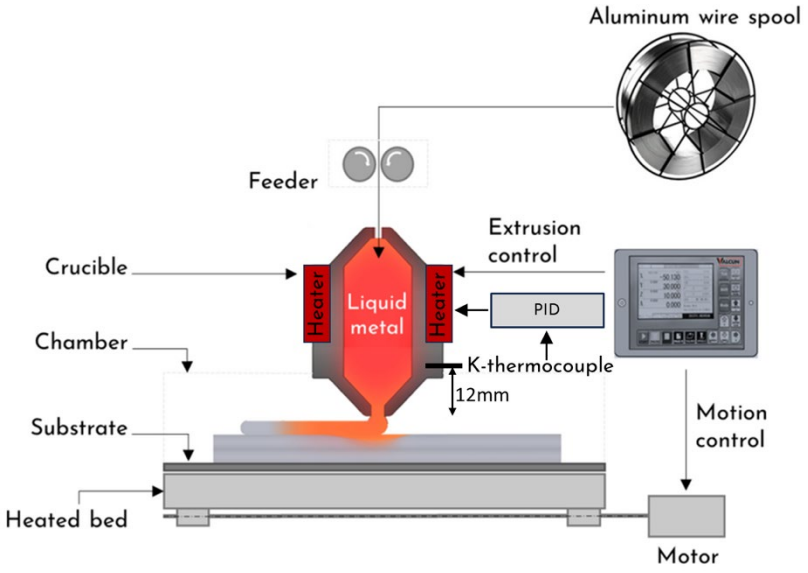


Figure 3.1. Schematic showing the components and procedures of molten metal deposition technique in which the real-time nozzle temperature is measured by K-type thermocouple [8].

Samples with a simple geometry, shown in Fig 3.2, were printed using a standard welding wire of a commercial 4043AM Al alloy under different process conditions. The nominal chemical composition (wt%) was: 5% Si, 0.08% Fe, 0.03% Cu, 0.002% Mn, 0.003% Mg, 0.002% Cr, 0.002% Zn, 0.014% Ti. Fig 3.3 is the photograph of top and side view showing an overall structure of one MMD sample. Overall, five samples (IDs R693, R688, R699, R748, R749) were fabricated by Valcun with controlled variation of nozzle temperature (525 – 970 °C), substrate temperature (500 – 644 °C), and printing speed (250 – 317 mm/min). These conditions were selected to manufacture samples with different geometries and microstructure based on their previous experience on printing materials with the technique. The coupled effect of the three conditions on various microstructural characteristics draws significant curiosity and demands great attention. The nozzle / substrate temperature of R748 were set at a fixed value to remain a consistent thermal load, and consistent printing speed for stable heat dissipation rate. Increasing parameters at the other four samples with different increments were designed to control the microstructure via manipulating the thermal conditions during processing. Table 3.1 summarise the printing conditions designed for each sample before fabrication. For all samples beside R748, the process parameters were changed uniformly according to printing height. For example, for R688, the printing started at 825 °C nozzle temperature, 500 °C substrate temperature and 300 mm/min printing speed. Then, after a build height of 10 mm had been reached, the nozzle and substrate temperatures were increased by 5 °C, and the printing speed by 1 mm min^{-1}, for every additional 5 mm of deposited height. Table 3.2 provides the sample dimensions of each sample. Fig 3.4 shows the evolution of the printing parameters during the experiment as well as real-time nozzle temperature against print height as measured by K-type thermocouple.

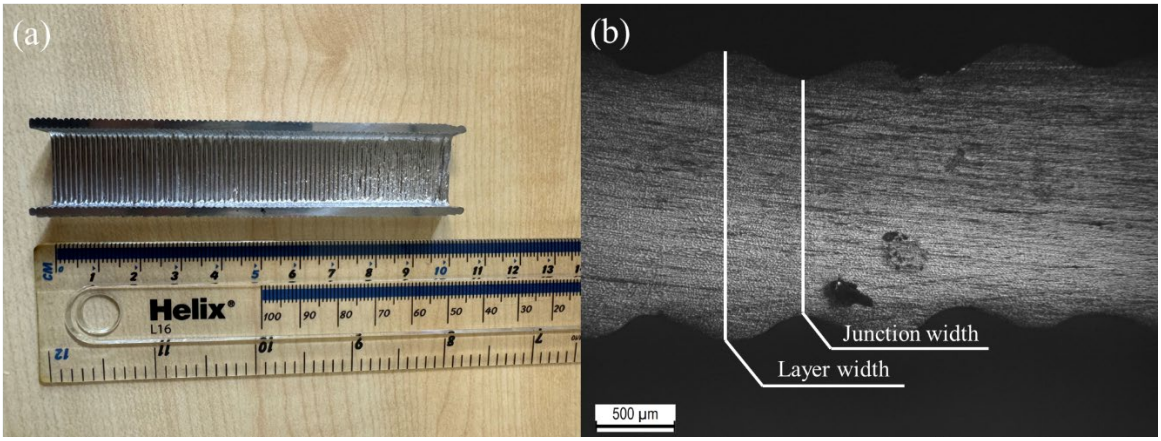


Figure 3.2. Images of sample R688 (a) full-length sample; (b) Optical micrograph showing the centre and junction widths.

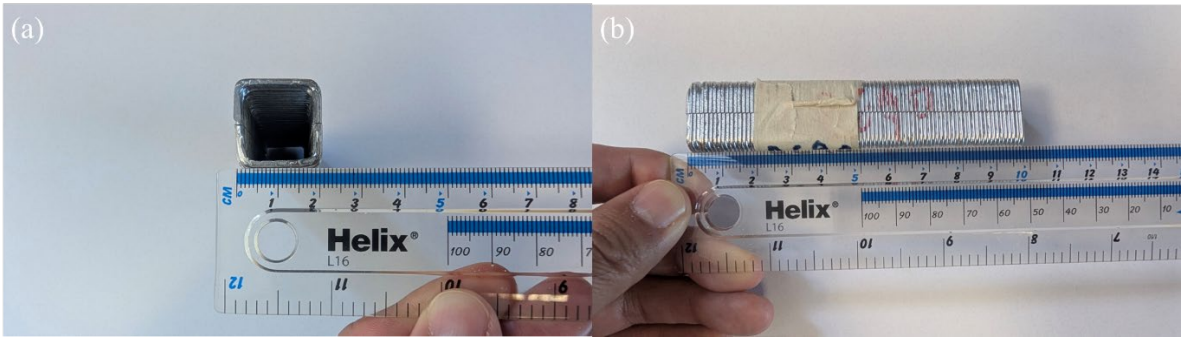


Figure 3.3. Photograph taken from the (a) top view and (b) side view of the MMD-processed sample.

Table 3.1. Printing conditions for each sample.

Sample ID	Printing speed (mm/min)	Nozzle temperature	Substrate temperature
R693	Start 250; 0.5 mm/min increment after z10	Start 825°C; 10°C increment after z25	Start 500°C; 10°C increment after z25
R688	Start 300; 1 mm/min increment after z10	Start 825°C; 5°C increment after z10	Start 500°C; 5°C increment after z10
R699	Start 250; 0.5 mm/min increment after z10	Start 825°C; 10°C increment between z25-65; 7°C increment between z65-100	Start 500°C; 10°C increment between z25-65; 7°C increment between z65-100
R748	300	825°C	500°C
R749	Start 250; 0.5 mm/min increment after z10	Start 825°C; 10°C increment after z30	Start 500°C; 10° increment after z30

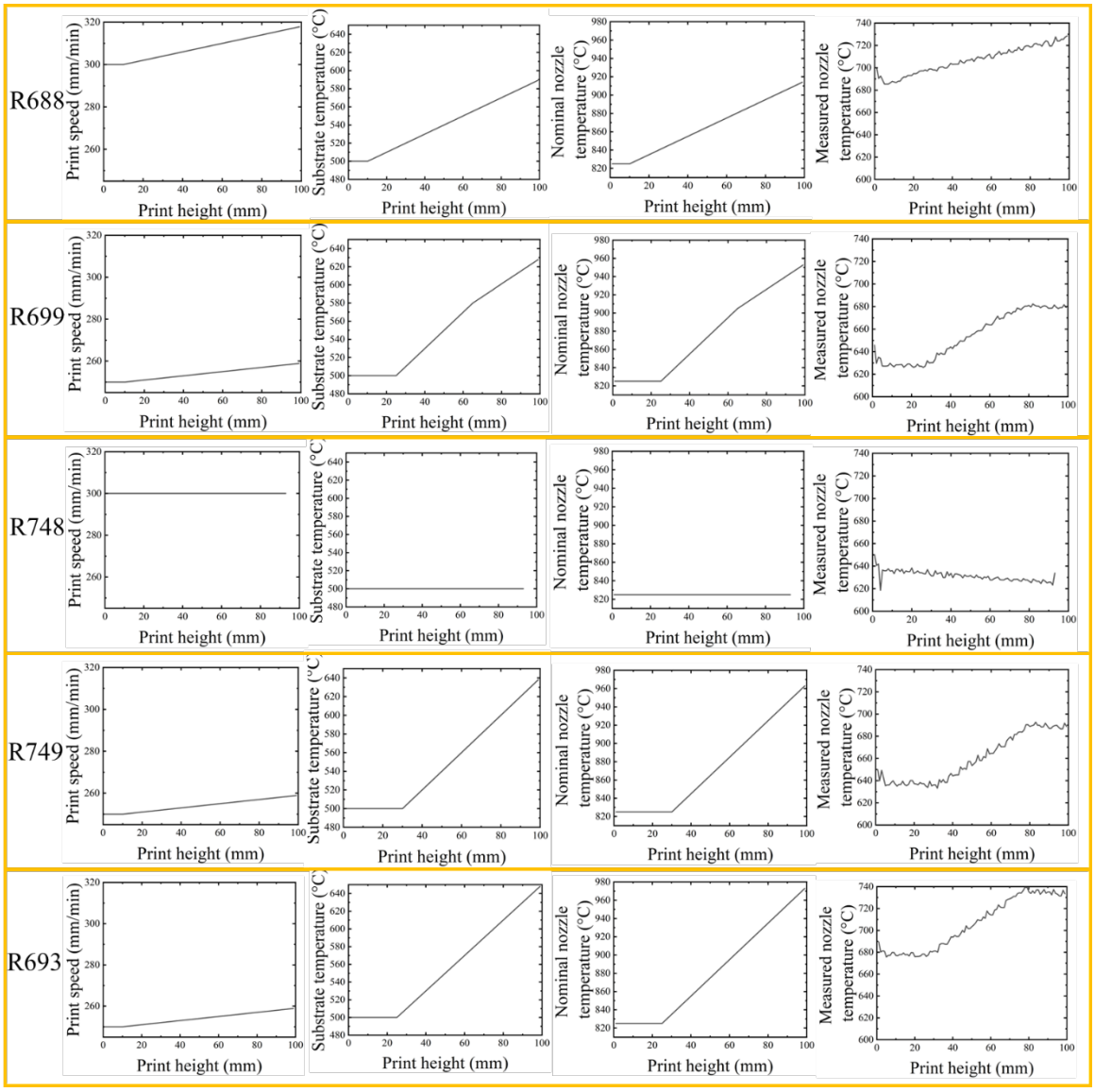


Figure 3.4. Printing parameters for the five samples: printing speed, substrate temperature, nominal nozzle temperature, measured nozzle temperature, for each sample as a function of print height.

Table 3.2. Sample dimensions including length, width, and height of each sample.

	Length (cm)	Width (cm)	Height (cm)
R688	2	2	9.95
R693	2	2	9.95
R699	2	2	9.95
R748	2	2	9.35
R749	2	2	9.95

3.2 Wedge casting

A cast bulk sample of 4043 alloy was prepared using a wedge Cu-mold shown in Fig 3.5. The nominal alloy composition (wt%) was: 5% Si, 0.08% Fe, 0.03% Cu, 0.002% Mn, 0.003% Mg, 0.001% Cr, 0.002% Zn, 0.014% Ti and balance Al. The wedge-mold allows to investigate solidification processes with cooling rate up to ~100 K/s, typical of many casting processes. The material was melted in a resistance furnace with air atmosphere within a crucible coated with a thin layer of Boron Nitride (BN) to protect from reacting with the liquid metal. The furnace temperature was set to 800 °C and the holding time was 2h. The wedge-mold had two overflow runners next to the cavity. The overflow runners routed the flow alongside the cavity to improve filling, and reduce turbulence and air entrapment [66].

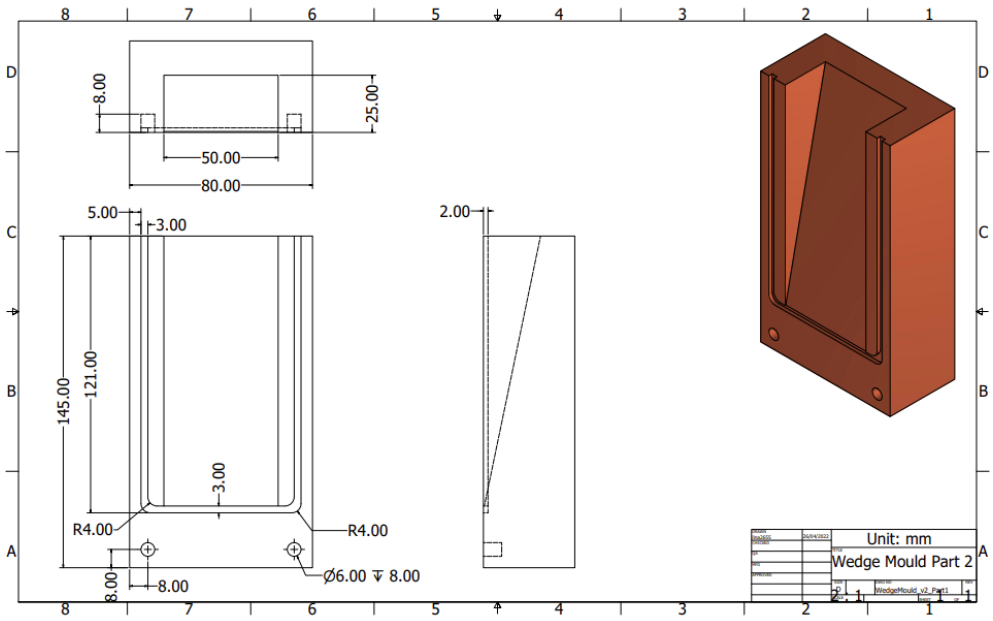


Figure 3.5. Schematic of half of the wedge mold showing the dimensions (in mm) used in this investigation.

The ingot was then cross-sectioned into five parts and marked as ‘tip a’, ‘tip b’, ‘middle’, ‘heel c’, and ‘heel d’, to observe the microstructure evolution under varying cooling rate. Thin plates were cut from the five parts to extract the alloy along the centreline.

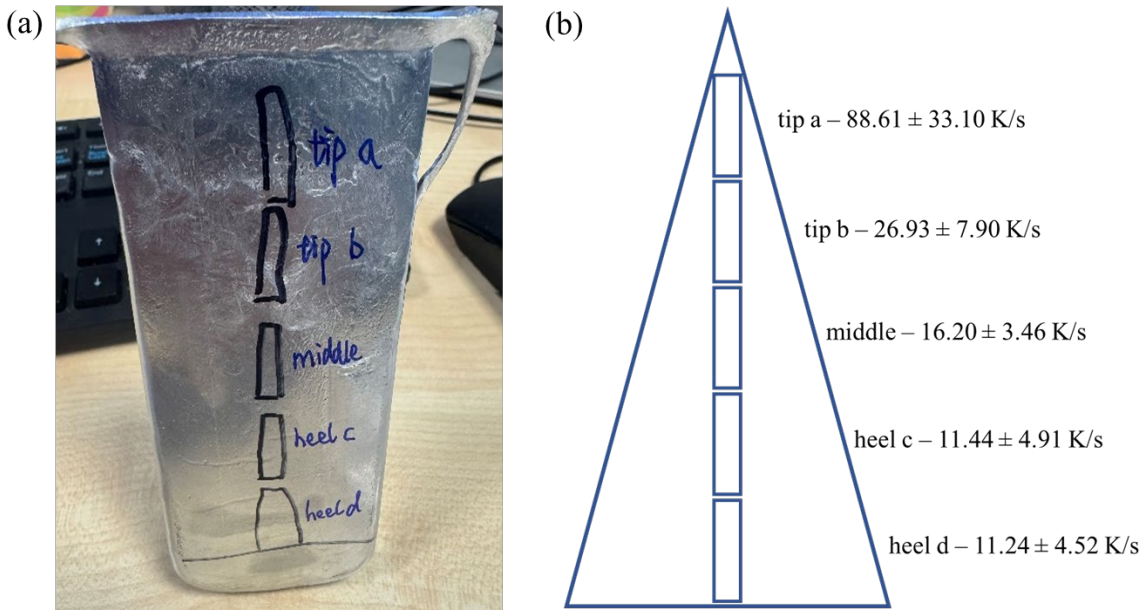


Figure 3.6. (a) the wedge-mold with labels of the five areas – tip a, tip b, middle, heel c, and heel d; (b) schematic showing the cooling rates within each region estimated from the SDAS analysis.

3.3 Metallographic preparation

Samples were sectioned, mounted (OPAL 460 Hot Mounting), grinded (Merkon Forcipol 300-IV Grinder-Polisher) and polished (ATM Saphir 330Twin grinder / polisher). Cross-sections of the MMD samples were taken to include the junction, centre, and edge regions for analysis. Samples were grounded with SiC papers up to a 4000-grit followed by polishing with 3 and 1 µm diamond suspension. Optical microscopy was utilized to ensure that the masks from previous grinding steps were removed. Ultrasonic cleaning with isopropanol for 5-10 minutes was performed between steps.

Optical microscopy (Polyvar) was used to measure junction and centre width from polished cross-sections using a ×5 magnification.

3.4 Electron microscopy

The microstructure of the junction, centre and edge regions of each layer was investigated using a JOEL-IT800 SEM with EDX. An in-column secondary electron detector (UHD), which is a high-efficiency detector for high resolution secondary electron imaging, was employed for surface morphological information of primary α-Al dendrites, Al-Si eutectic, pure Si particles,

and Fe-rich IMCs. The super hybrid lens (SHL) mode at a working distance (WD) of 5 mm was selected for UHD. The standard mode of probe size (probe current 50) was selected. The voltage of the incident electron beam was set to 5 kV. Different magnification (Mag) at 300, 800, 3k, and 6k, were used for step-wise close observation on morphology of different phases. A scintillator backscatter electron detector (SBED) was utilized to give a better contrast on different phases, *e.g.,* Si and Fe-rich IMCs. The standard mode (STD) and WD of 10 mm were used. Three regions were selected for electron microscopy on each sample to represent the morphological difference across one layer. Fig 3.7 shows sample R748 as an example where an OM image of consecutive layers and corresponding EM images at three regions are shown.

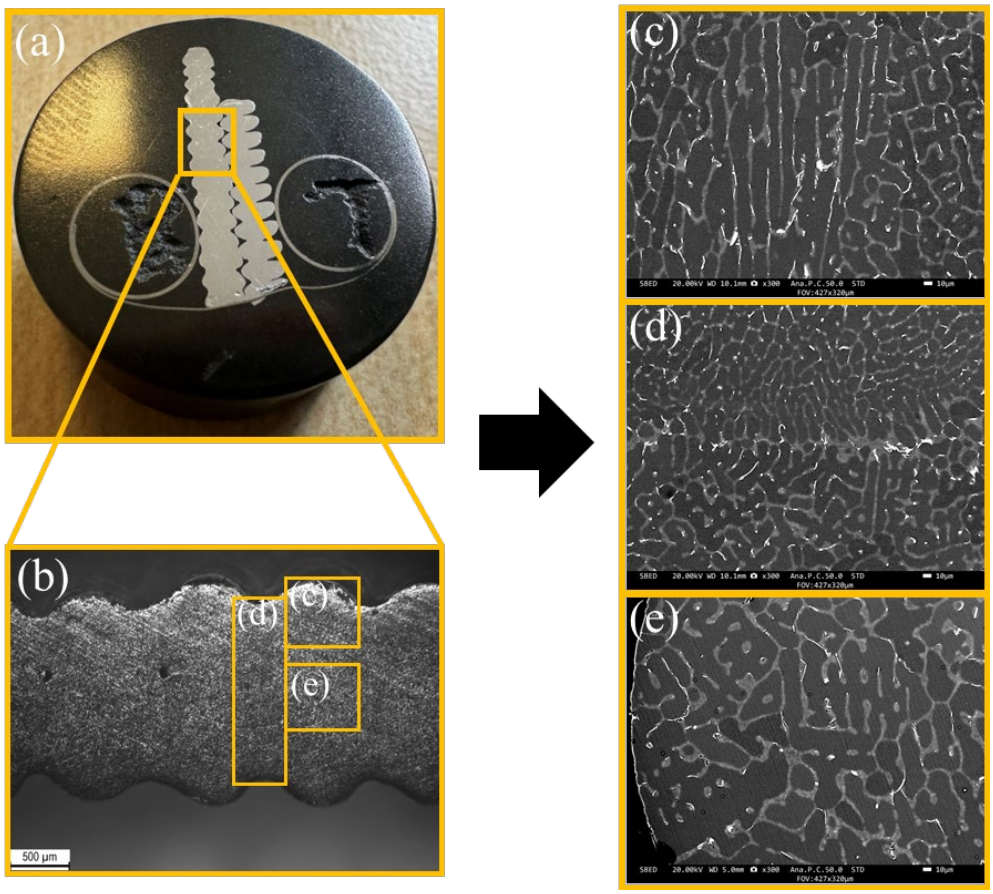


Figure 3.7. Three regions selected for electron microscopy, representing the morphological characteristics, on sample R748: (a) centre region; (b) junction region; (c) edge region.

3.5 Sample geometrical consistency measurement

The images of centre and junction regions of each layer were firstly obtained using OM and imported into ImageJ for measurement. The width of centre and junction region of the five samples was measured, respectively, and the average and standard deviation were compared to estimate the degree of liquid spread and remelting during deposition.

3.6 IMC morphology analysis

Fig 3.8 shows the processing procedure of the SEM images. The segmentation of IMCs on SEM images and measurement of their area, area fraction, aspect ratio, length, and width were done using a Bespoke Matlab script provided by Dr. Shikang Feng. The images at junction and centre regions of each layer on R693, R699, and R749, as well as selected layers on R688 and R748, were processed.

The raw SEM images were firstly converted to greyscale, and then normalised, i.e. rescaled between 0 and 1. Because SEM images after different acquisition processes may have different contrast, the normalization reduce the sensitivity of the subsequent segmentation to acquisition conditions.

A bilateral filter was then applied to reduce noise. The filtered images were then segmented using a k-means clustering algorithm, which divided pixels into four groups of different phases (Al, Si, and Fe-rich intermetallics) based on intensity similarity. During K-clustering, each pixel is assigned a cluster label, *e.g.,* 1,2, and 3, and IMCs were isolated from the matrix. A binary mask of the IMC was thus created keeping only the cluster with the corresponding label. Small detected objects were subsequently removed using an area filter, with the threshold value associated with the pixel sizes, so that all connected components that have fewer than 36 pixels are discarded (corresponding to approx 1 μm^2). To characterize the geometric and

morphological properties of the segmented IMCs, the x-y coordinates, area, major and minor axis, and the area fraction were measured from the binary mask of the IMCs.

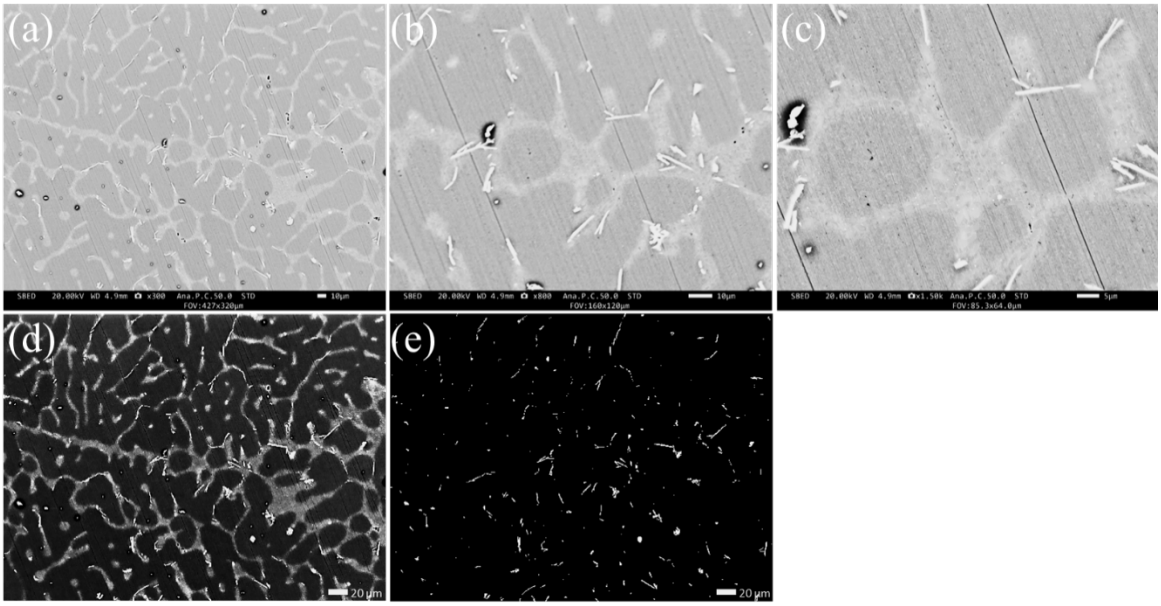


Figure 3.8. Demonstration of the procedure of image processing (a)(b)(c) image normalization at different Mag; (d)(e) image segmentation using the binary mask of the selected cluster of IMCs.

3.7 Grain size measurement

Grain size measurement was performed manually using ImageJ, by measuring the transversal and longitudinal interior section-lines of each grain on SEM micrographs. The grain size measurement procedure suing ImageJ is given in Fig 3.9.

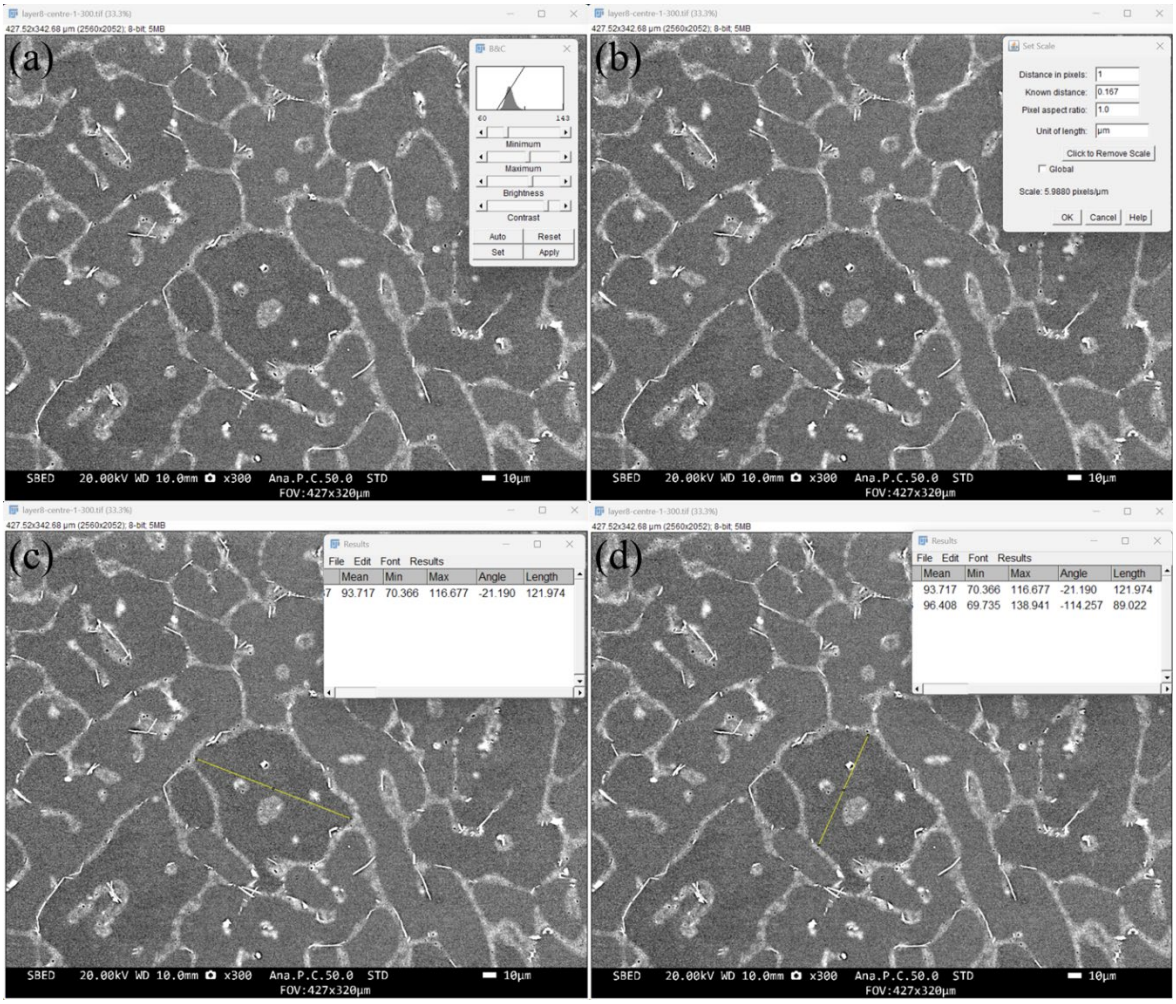


Figure 3.9. Grain size measurement using ImageJ: (a) thresholding; (b) set scale; (c) the transversal interior sectionline measurement; (d) the longitudinal interior sectionline measurement.

3.8 SDAS measurement

The α-Al dendrites typically contained two to four secondary dendritic arms, allowing secondary dendrite arm spacing (SDAS) to be measured. SDAS was used to estimate the local cooling rate. For each sample position, six micrographs were selected, and ten dendrites were measured in each image. SDAS measurements were performed using ImageJ software [67]. For each dendrite, the measurement was taken across three or more secondary dendrite arm spacings using an edge-to-edge method. The SDAS was calculated as the ratio of the measured dendrite length, (L), to the number of secondary dendrite arm spacings, (N), according to equation 1 [67]:

$$SDAS = \frac{L}{N} \quad (1)$$

The corresponding cooling rate was then estimated using the empirical relationship shown in equation 2 [67]:

$$Cooling\ rate = (\frac{SDAS}{B})^{-\frac{1}{n}} \quad (2)$$

where (B) is an alloy-specific fitting factor and (n) is a constant. For 4043 Al alloy, B = 50 μm $(Ks^{-1})^n$ and n = 0.33, a unitless number [67].

3.9 Porosity

Pores were observed at the geometry measurement using OM and sample preparation process for SEM. During assessment on surface finish using OM after each step, it was observed that the mechanical deformation at the polishing of mounted samples using diamond suspension with different SiO_2 particle size and subsequent ultrasonic cleaning tend to enlarge the pores at the surface of the samples. SEM is considered not applicable for porosity measurement and it is not included in this work.

Chapter 4

MMD microstructure of a 4043 Al alloy

This chapter examines the microstructure of 4043 Al alloy components produced by molten metal deposition (MMD) using a ValCUN system under different combinations of printing speed, nozzle temperature and substrate temperature. The aim is to establish how these processing conditions influence dimensional stability, junction formation, solidification morphology and the distribution of Fe-rich intermetallic compounds (IMCs). SEM observations are combined with quantitative image analysis in MATLAB to measure IMC area fraction, size, aspect ratio and spatial distribution, while grain size and secondary dendrite arm spacing (SDAS) measurements are used to estimate local cooling rates. To separate the effect of cooling rate from the specific geometry of the MMD process, the MMD microstructures are also compared with wedge-cast 4043 Al alloy produced from the same composition. Overall, the chapter shows that MMD produces a relatively continuous and near-isotropic Al-Si dendritic microstructure, with limited melt-pool-like boundary contrast, locally enriched eutectic regions at interlayer junctions, and finely dispersed Fe-rich IMCs whose morphology is governed primarily by cooling rate and thermal exposure.

4.1 Results

4.1.1 MMD samples

Dimensional consistency

The measurements of junction and centre width, and their ratio are shown in Fig 4.1. The junction width varied between 1176 ± 285 µm (R748) and 1430 ± 130 µm (R699), while centre width was between 1750 ± 102 µm (R699) and 1860 ± 68 µm (R749). Fig 4.1 also shows that R693, R688 and R699 had a similar junction / centre ratio of approximately 0.8, whereas R749 and R748 had a lower ratio.

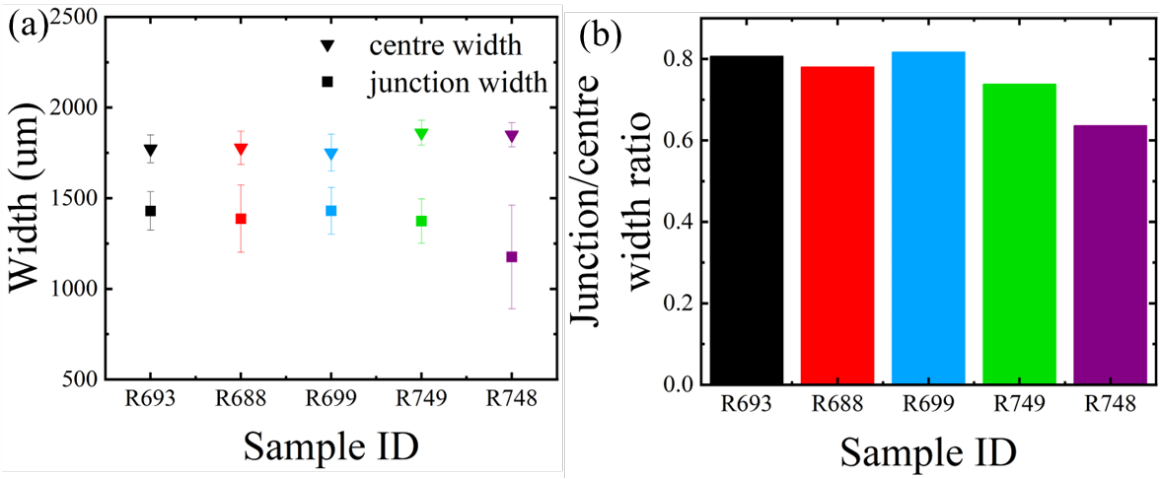


Figure 4.1. (a) junction and centre width of sample R693, R688, R699, R749 and R748; and (b) ratio.

Fig 4.2 shows the width layer by layer for all samples. The junction widths were comparatively similar before layer 40, whereas, R748 and R688 showed a prominent decrease in the subsequent layers, while R693, R699 and R749 remained unchanged. On the other hand, the centre widths were broadly similar within the entire samples.

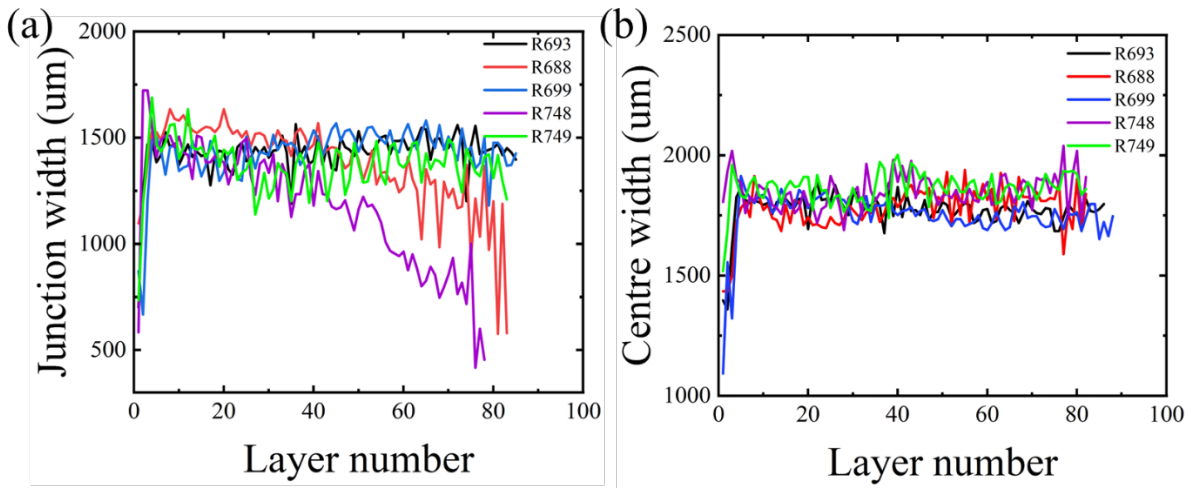


Figure 4.2. (a) junction width and (b) centre width plotted as a function of layer numbers. Numbers of each top layer with their corresponding stack height: R693 – 99.49 mm; R688 – 99.5 mm; R699 – 99.51 mm; R748 – 93.51 mm; R749 – 99.51 mm.

Microstructure

Fig 4.3 shows a representative deposited layer from sample R693. The overview image in Fig 4.3(a) identifies the centre of the layer, located between two interlayer junctions formed by successive deposition passes. The microstructure is dendritic, with Al-Si eutectic and Fe-rich IMCs located mainly along interdendritic regions and grain boundaries. The Al nuclei formed in the liquid metal and the primary dendrites grew uniformly in all directions. For the nuclei with an equal size in all directions in 3D space, it is named equiaxed. Whereas, grains with a preferential growth direction, it is named columnar. The columnar grains in the centre of Fig 4.3 (b) grew in a direction of heat extraction which is vertical to the substrate, but the amount can be considered as minority compared with the overall equiaxed morphology of the sample. The overall equiaxed structure offers the material with equivalent mechanical properties in all directions which is known as isotropy. Layer number of the five samples ranges between 70 – 80, SEM images were taken from bottom to top layers in the direction parallel to the build direction. The bottom, middle, top regions correspond with layer 1 – 30, 31 – 60, and 61 – top layer, respectively. Equiaxed Al dendrites at centre show a decreasing in size and dendritic arm

spacing as stack height increasing. At the junction, shown in Fig 4.4, the eutectic network and bright Fe-rich IMCs are more clearly resolved.

The higher-magnification images in Fig 4.4 clarify the phase distribution within a junction region. The Al-Si eutectic is finely dispersed within the interdendritic channels (Fig 4.4(c)), while the Fe-rich IMCs are small, discontinuous and closely associated with the eutectic (Fig 4.4(d)). The eutectic Si is also very fine, with submicrometre-scale features visible in Fig 4.4(c) and (d).

Fig 4.5 compares junction regions from different samples and build heights. Si-rich segregation is observed at the junctions in all samples; however, these enriched regions are relatively localised and do not form a macroscopic discontinuity. No pronounced anisotropy or fully columnar morphology is evident in the α-Al dendritic/grain structure across the junctions. The electrons collected by the BSE detector consist of the incident electrons elastically backscattered by the atomic nuclei and inelastically backscattered by the outer shell atoms. The intensity of the signal depends on the probability of material atoms backscattering incident electrons which is determined by the atomic number. The IMCs commonly observed in 4043 Al alloys are α-Al_8Fe_2Si with 25.6 wt% Fe and 12.8 wt% Si, and β-Al_5FeSi with 15.7 wt% Fe and 7.9 wt% Si. The atomic number of Al, Si, and Fe were 13, 14, and 26, respectively. Thus, with a higher content of Fe, α-Al_8Fe_2Si often shows a higher contrast on BSE images. Additionally, based on Fig 4.3(b), IMCs are mostly α-Al_8Fe_2Si with Chinese-script morphology, along with a few β-Al_5FeSi with needle-like morphology in 2D. Thus, the IMCs in MMD-processed 4043 Al alloy can be considered as a mixture of α and β phases.

Fig 4.6 presents a corresponding collage of centre-region microstructures from the different samples and build heights. Although variations in dendritic arm spacing can be observed, the centre regions generally retain a comparable α-Al dendritic/cellular morphology with fine

interdendritic eutectic and IMCs, indicating that the microstructure is comparatively homogeneous across the sampled conditions.

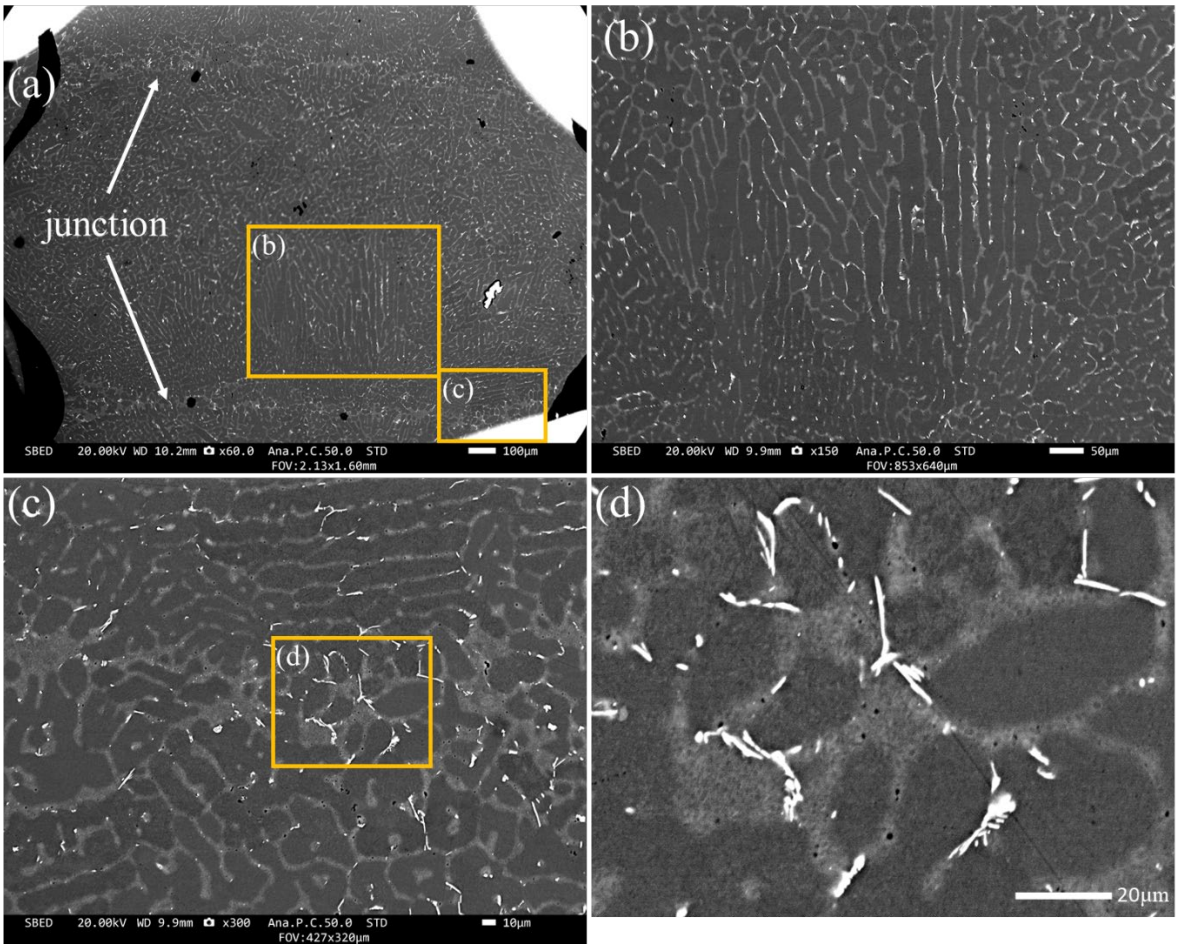


Figure 4.3. SEM images of centre and junction regions at layer22 of sample R693 showing layer structure: (a) overview of one layer; (b) centre region; (c) junction region; (d) IMC concentration at the junction where IMCs were identified as phase in white by BSE detector.

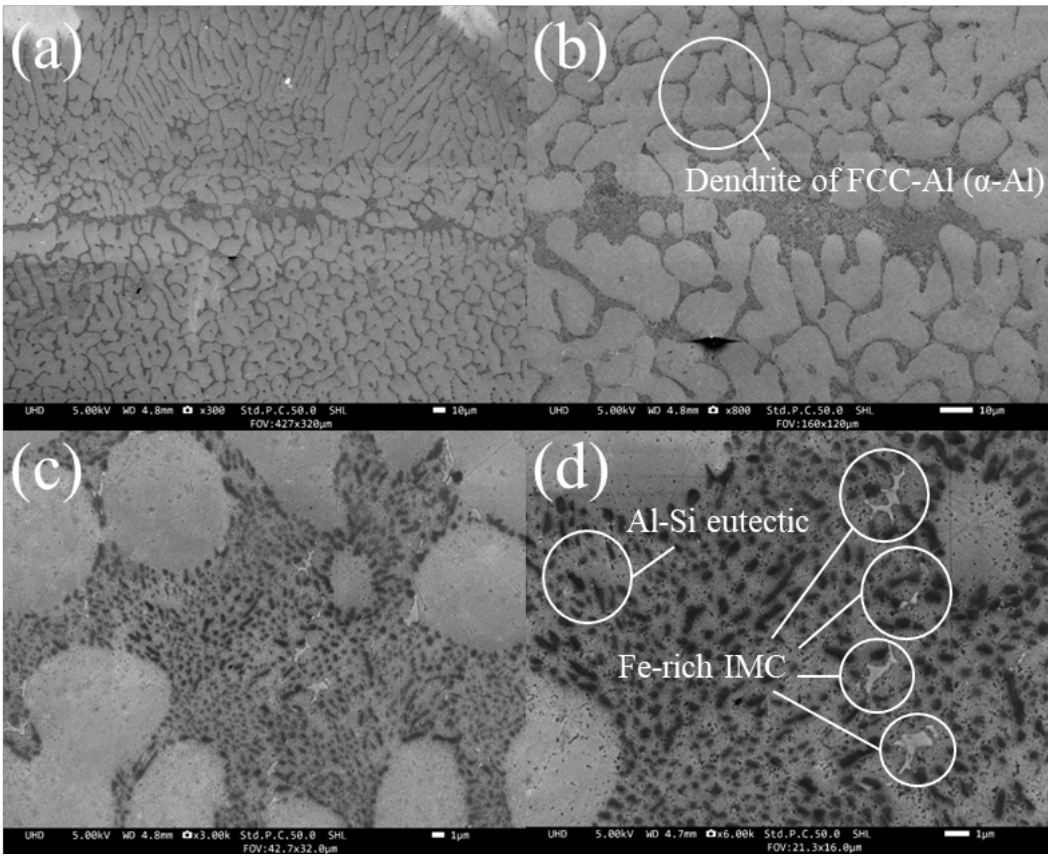


Figure 4.4. Junction area by secondary electron signal (UHD detector) at layer78 of R748 at different magnification showing Al-Si eutectic network (a): × 300; (b): × 800; (c): × 3k; (d) × 6k.

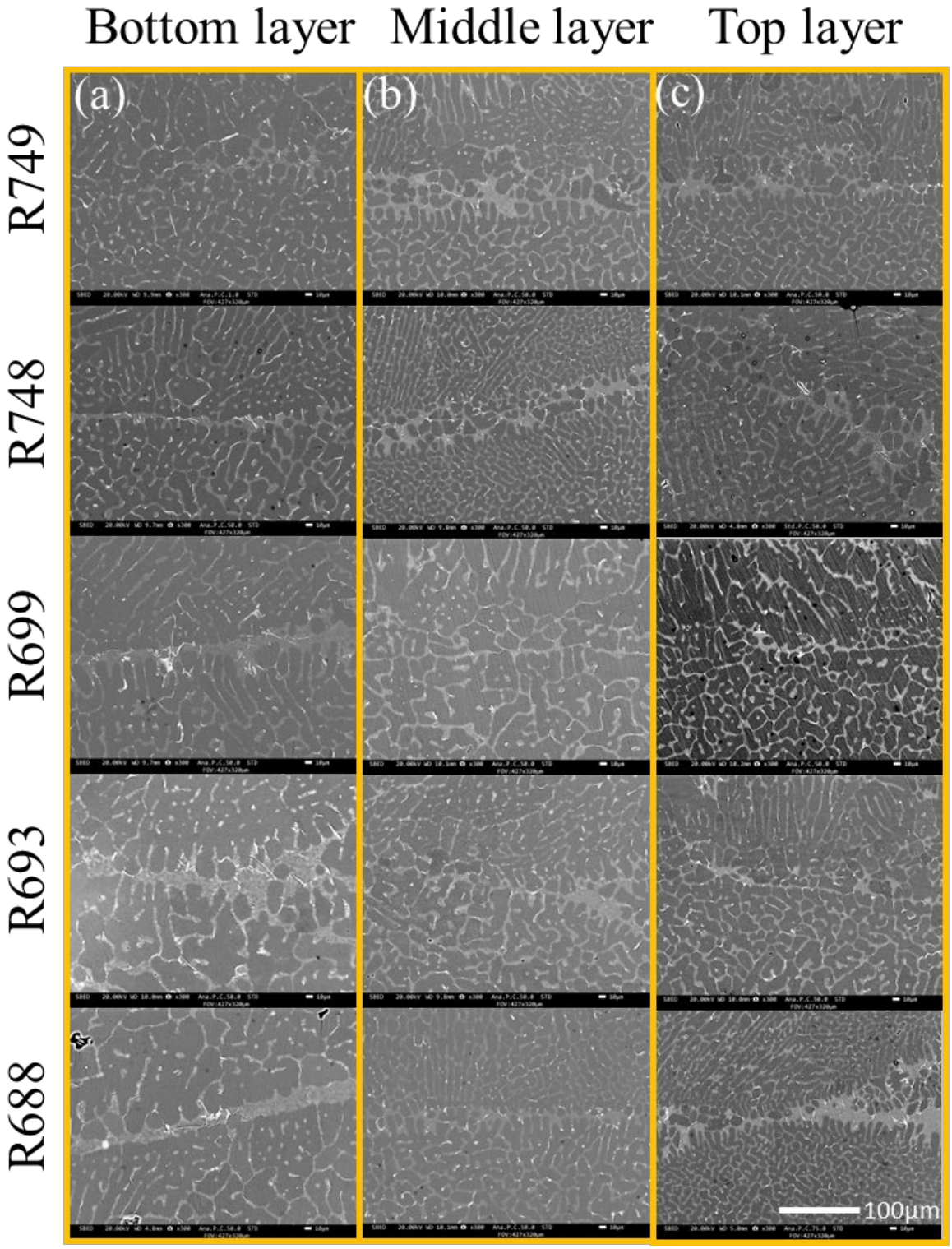


Figure 4.5. SEM images by backscatter electron signal (SBED detector) from bottom, middle, and top layers of each sample junction at 300 Mag (a) column for bottom layer; (b) column for middle layer; (c) column for top layer of the print.

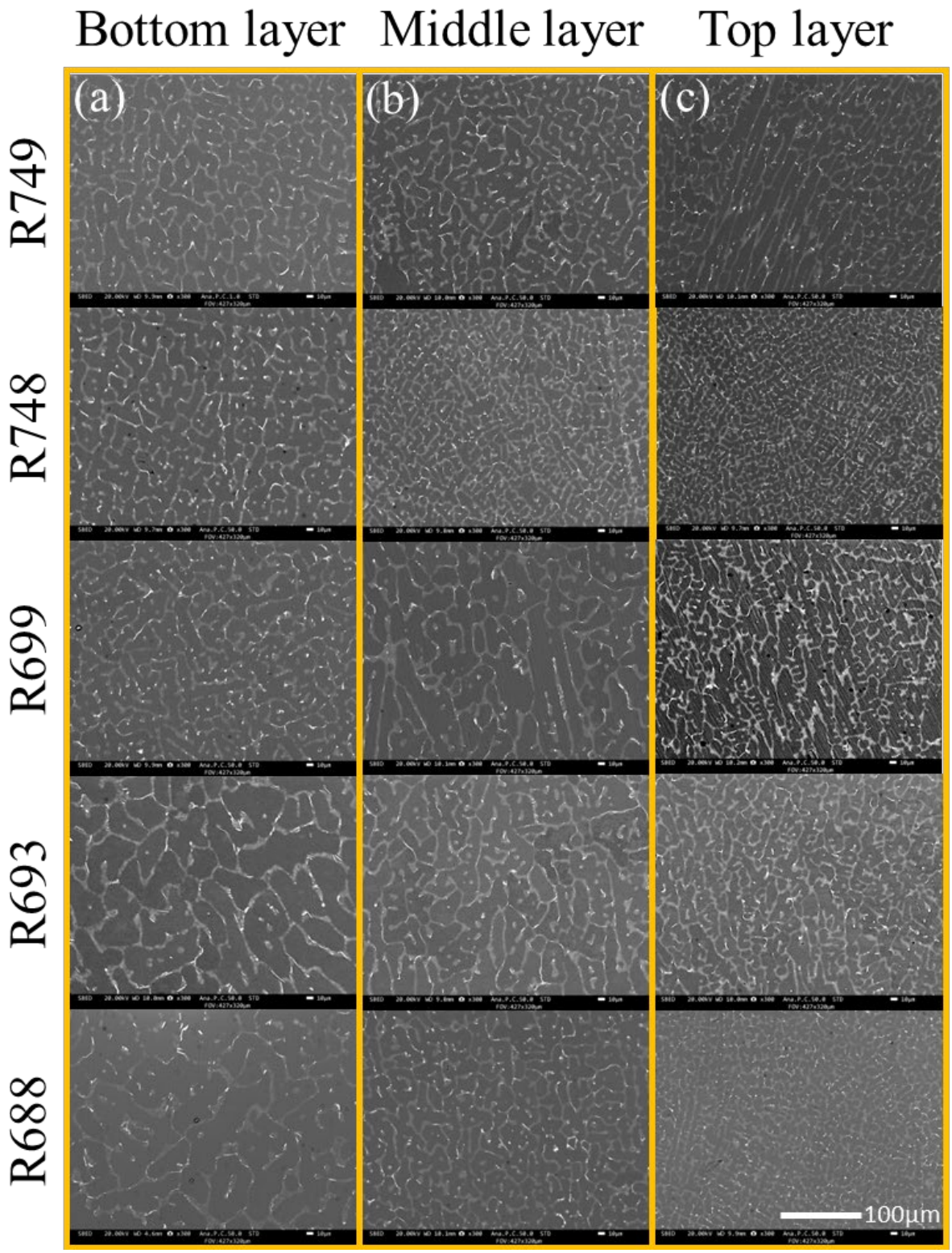


Figure 4.6. SEM images by backscatter electron signal (SBED detector) from bottom, middle, and top layers of each sample centre at 300 Mag (a) column for bottom layer; (b) column for middle layer; (c) column for top layer of the print.

Grain size analysis

Grain size was measured manually for selected layers in two representative samples, R688 and R748, while SDAS was measured across a larger number of layers for all samples. The grain-size measurements therefore provide direct evidence of the α-Al grain morphology in selected regions, whereas the SDAS measurements provide a broader indication of the evolution of solidification conditions through the build. As summarised in Fig 4.7, R688 showed a reduction in average grain size from 99.55 ± 39.73 μm in the lower and middle regions to 30.01 ± 12.44 μm in the top layers, together with a narrower grain-size distribution. R748 showed a similar refinement towards the top of the build, with the average grain size decreasing from 76.91 ± 45.20 μm in the middle region to 47.62 ± 18.52 μm at the top.

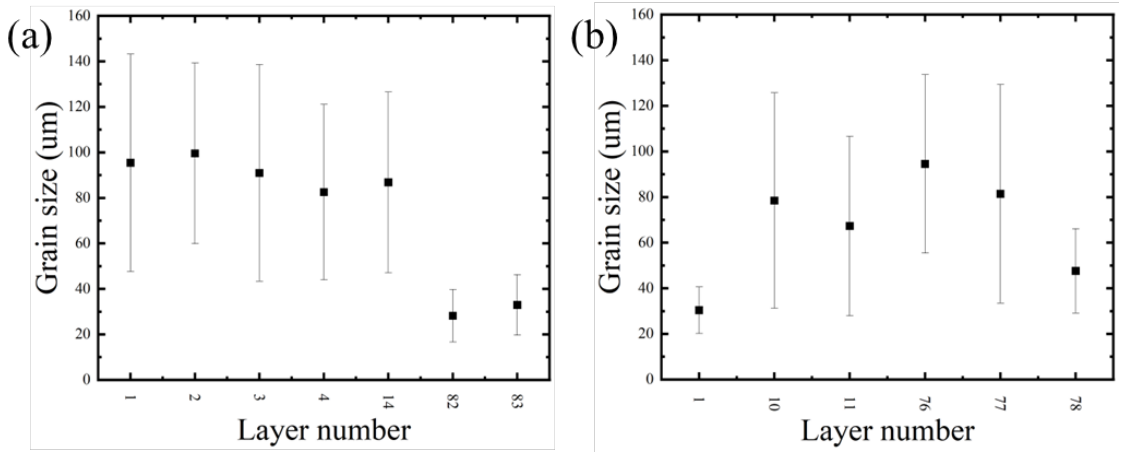


Figure 4.7. Comparison of grain size of (a) R688 and (b) R748.

The layer-by-layer grain-size distributions for R688 are shown in Fig 4.8. The bottom layers (layers 1-4) exhibited a broad distribution from approximately 20 to 200 μm, with number-fraction peaks at 60-80 μm and 100-120 μm, indicating relatively coarse primary α-Al grains. A similarly broad distribution was observed at the middle height (layer 14), where the maximum number fraction occurred at 80-100 μm. In contrast, the top layers (layers 82 and 83) showed a much narrower distribution of approximately 10-80 μm, with peaks at 20-30 μm and 30-40 μm, confirming grain refinement near the top of the build.

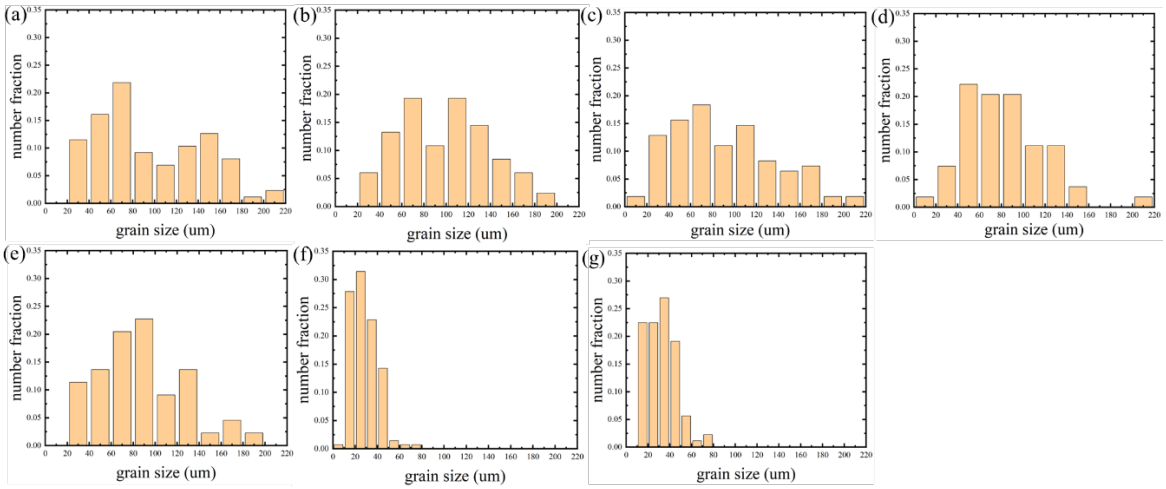


Figure 4.8. Measurement of grain size of R688 (a) layer1; (b) layer2; (c) layer3; (d) layer4; (e) layer14; (f) layer82; (g) layer83.

For R748, shown in Fig 4.9, layer 1 at the bottom of the stack exhibited a fine grain-size distribution of 10-60 µm, with a peak at 30-35 µm, representing the finest microstructure within the sample. At the middle height (layers 10 and 11), the distribution broadened to approximately 25-175 µm, with peaks at 25-35 µm and 45-65 µm. Towards the top of the build, the distributions shifted again towards smaller grain sizes: layers 76 and 77 showed ranges of approximately 20-160 µm and 10-175 µm, respectively, while the top layer 78 showed a finer distribution of 10-70 µm.

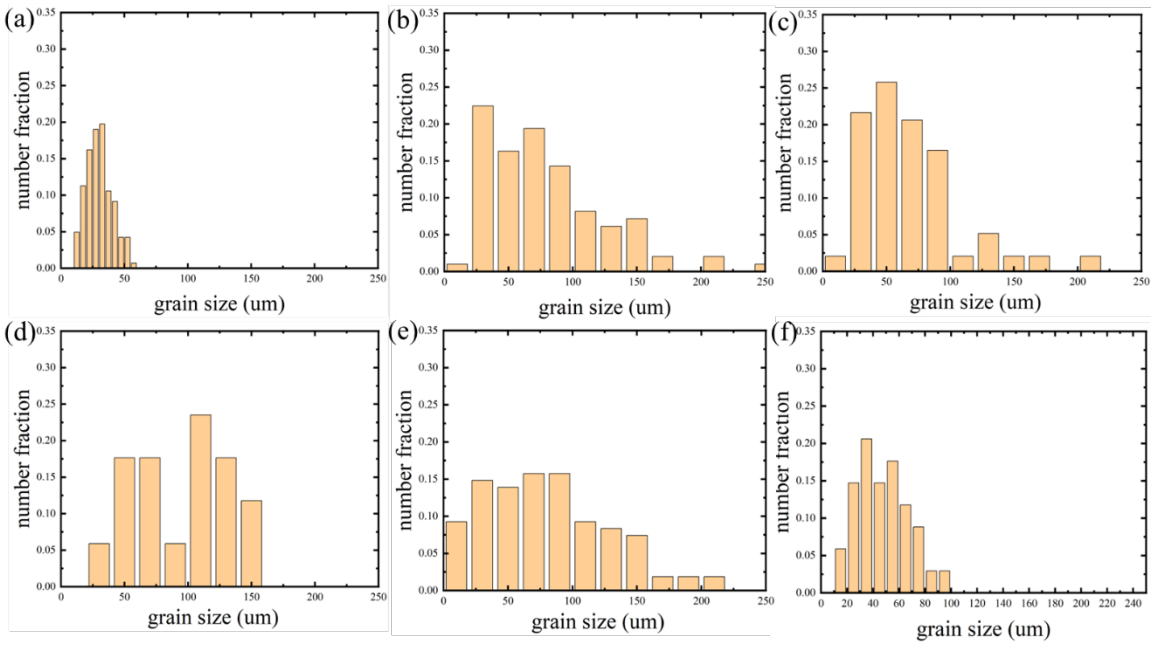


Figure 4.9. Measurement of grain size of R748 (a) layer1; (b) layer10; (c) layer11; (d) layer76; (e) layer77; (f) layer78.

The broader SDAS measurements in Fig 4.10 support the grain-size observations of decreasing grain size as stack height increasing, with decreasing space of interdendritic channel as layer number increasing, but also reveal additional detail. In most samples, SDAS initially increased during the first 10-20 layers, reaching approximately 30-40 μm, before decreasing to below 20 μm in the upper layers. This trend was observed in both the centre and junction regions, although the junction region consistently showed slightly smaller SDAS values, typically by about 2-3 μm. This indicates that the local solidification conditions evolved with build height and were slightly different between the centre and junction regions.

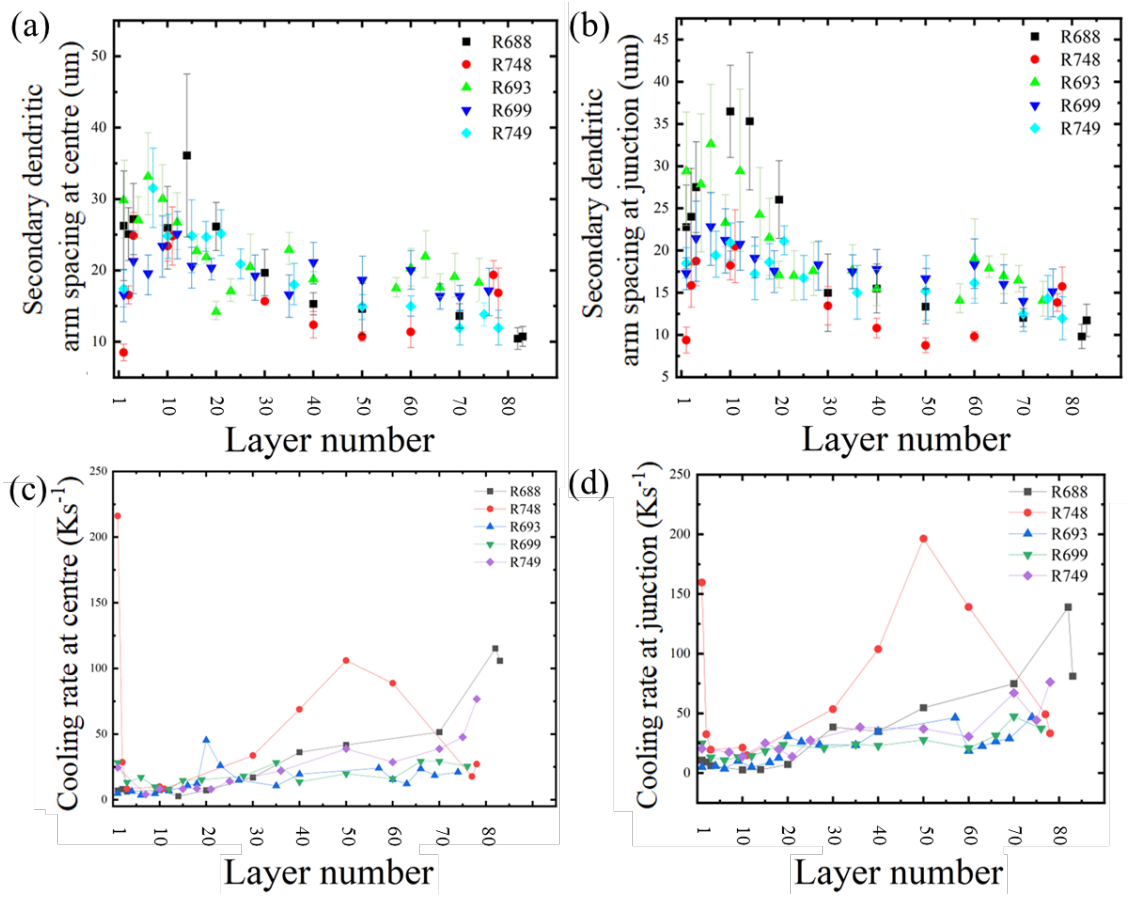


Figure 4.10. (a) SDAS at centre region; (b) SDAS at junction region; (c) cooling rate at centre region; (d) cooling rate at junction region as a function of layer number.

IMC size and morphology

Fig 4.11 presents the layer-by-layer IMC measurements for the junction regions of all five samples. In general, coarser IMCs were observed near the bottom and middle of the builds,

whereas finer IMCs were more common towards the upper layers. This trend was sample dependent. For example, R748 already exhibited relatively small IMCs at layer 1, with an average overall area of 0.594 μm² and an aspect ratio of 2.277, while the top layer of R749 showed lower IMC dimensions than its lower layers.

The overall IMC area in R748 and R688 decreased progressively from the bottom to the top layers. In contrast, R693, R699 and R749 showed a decrease in IMC area up to approximately layers 20-30, followed by relatively stable values.

Figs 4.12 and 4.13 present the IMC distributions within each sample for the centre and junction regions, respectively. Overall, the size and morphology of the IMCs were broadly consistent across the five samples and between the two regions.

Fig 4.14 summarises the average IMC measurements for all five samples. The IMCs were finely dispersed, with median lengths of approximately 2-5 μm. Subtle sample-to-sample differences were observed: R688 exhibited the largest IMCs, whereas R748 showed the smallest average IMC area (Fig 4.14(a)); however, the average area remained below approximately 3 μm² in all samples. R688 had the lowest IMC area fraction, approximately 0.5%, while R699 had the highest, approximately 0.9%. R688 also showed the highest aspect ratio and the largest variance, although the average aspect ratios remained close to 3 for all samples. Similarly, IMC length and width were greatest in R688, but the differences between samples were modest, generally within approximately 2 μm. In processing of images, small detected objects were removed by an area filter which discarded connected components with pixel number smaller than 36. Area fraction was subsequently derived from the result of the overall area of IMCs devided by the area of the image segmented. Thus, regarding the different area fraction between five samples, one possibility is that the detected small IMCs solidified at high cooling rate contains less than 36 pixels in the image and were removed by the filter.

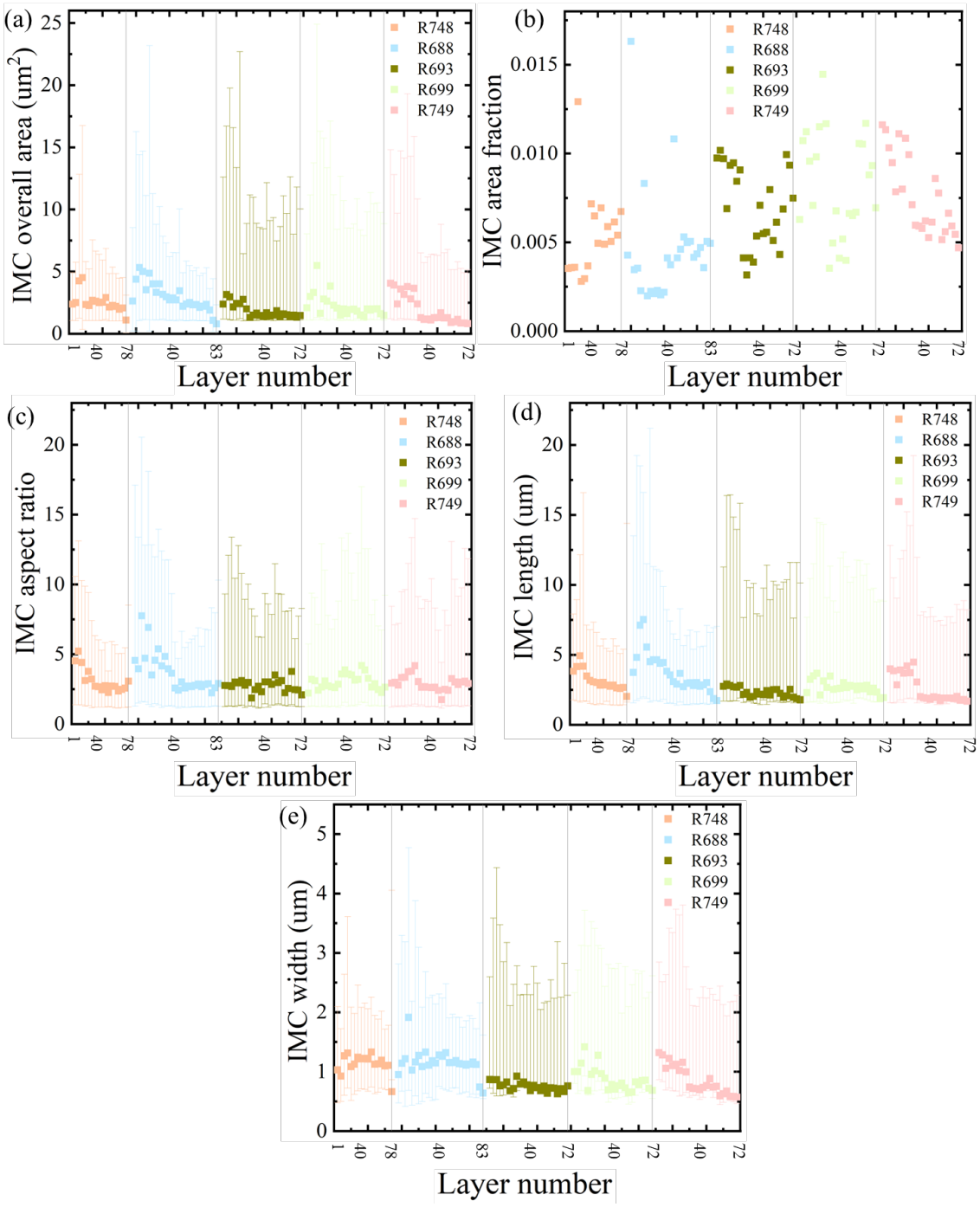


Figure 4.11. IMC phase measurements of junction region of all five samples with corresponding nozzle temperatures of each layer (a) overall area; (b) area fraction; (c) aspect ratio; (d) length; (e) width.

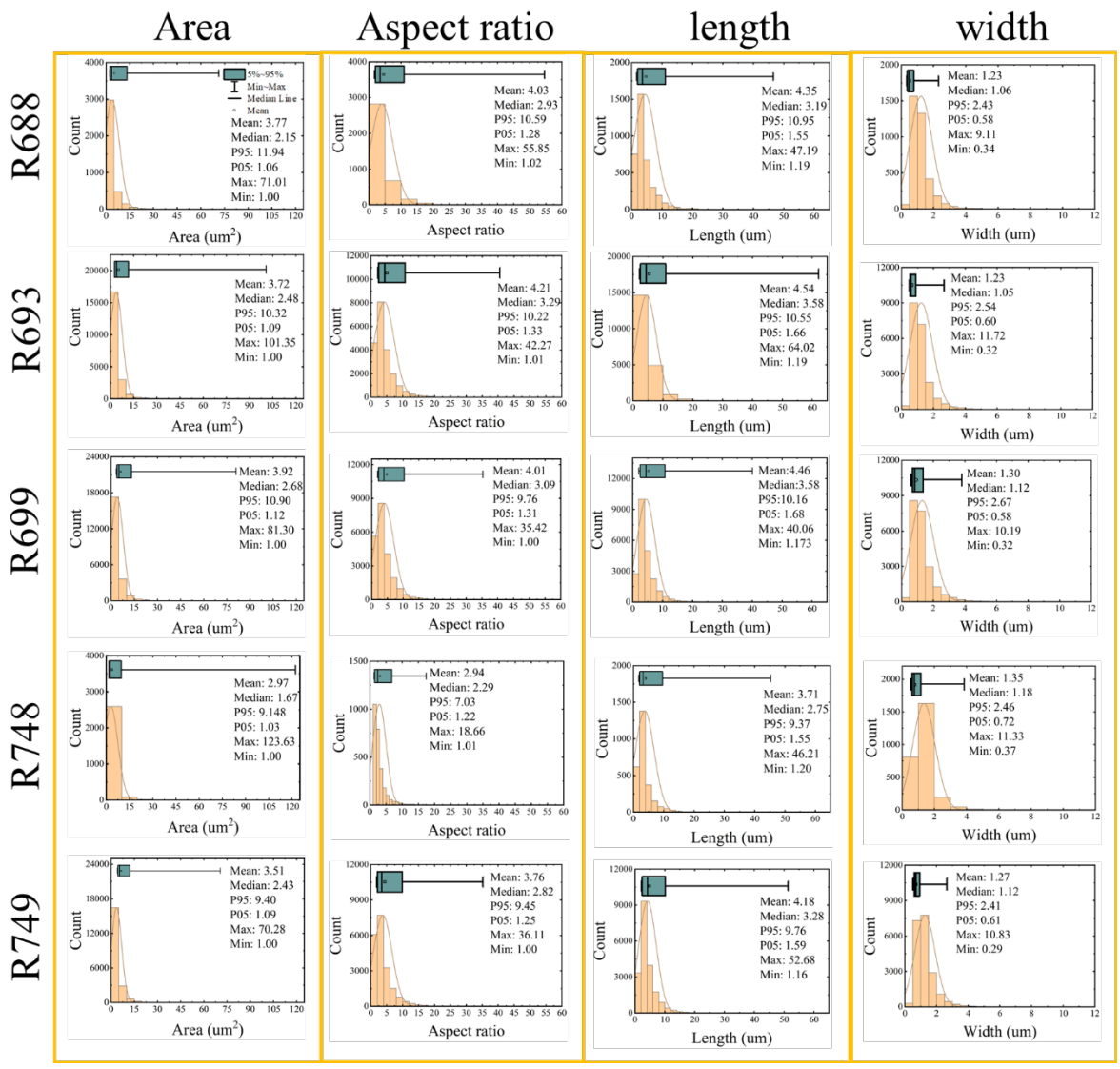


Figure 4.12. Sample-by-sample variance of IMC area, aspect ratio, length, and width distribution at centre region. Percentile 0.95 (P95) and 0.05 (P05) of IMC measurements of each layer were derived. P95 – mean and mean – P05 were plotted as upper error and lower error, respectively. (a) column for area; (b) column for aspect ratio; (c) column for length; (d) column for width.

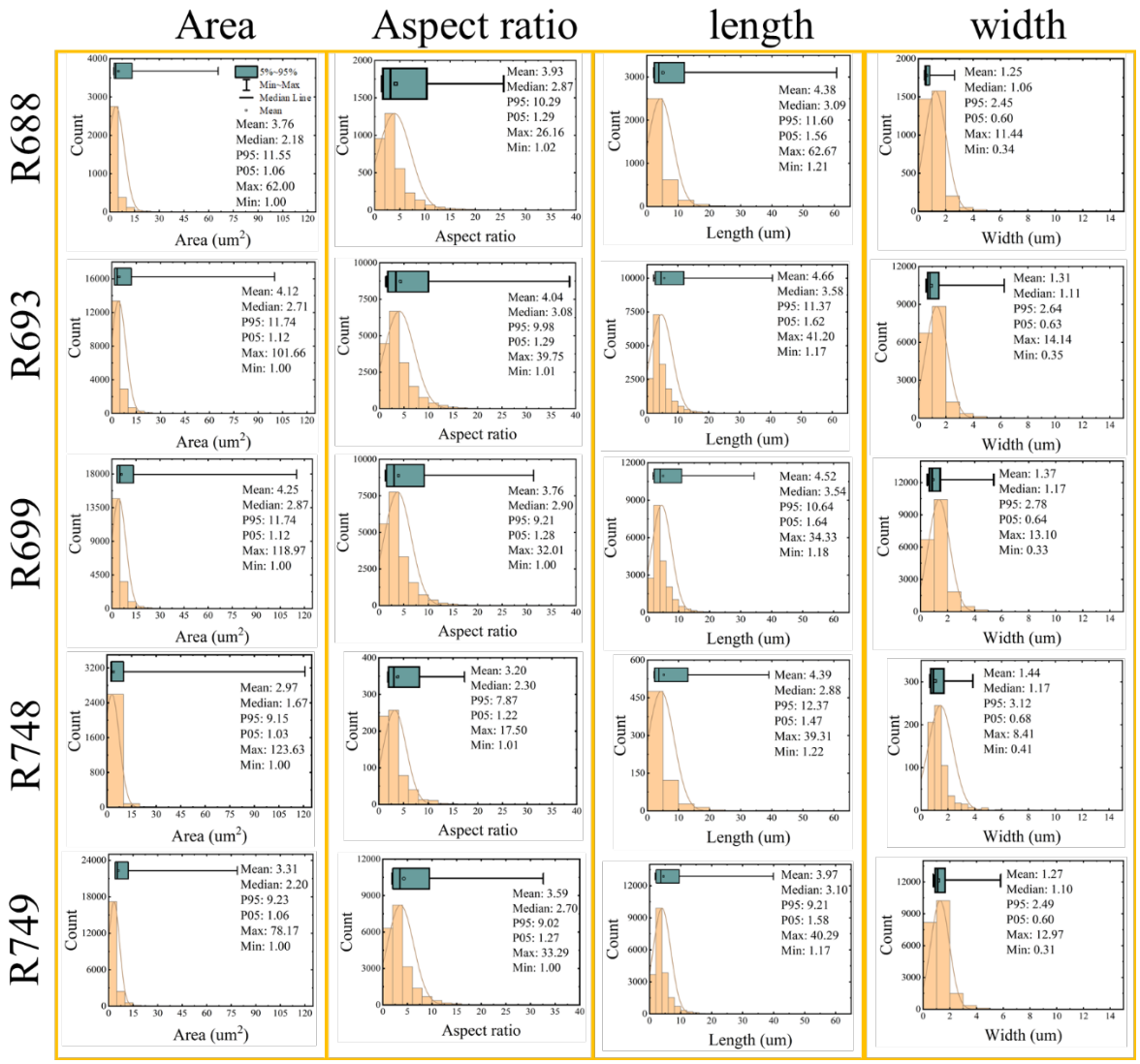


Figure 4.13. Sample-by-sample variance of IMC area, aspect ratio, length, and width distribution at junction region. Percentile 0.95 (P95) and 0.05 (P05) of IMC measurements of each layer were derived. P95 – mean and mean – P05 were plotted as upper error and lower error, respectively. (a) column for area (b) column for aspect ratio; (c) column for length; (d) column for width.

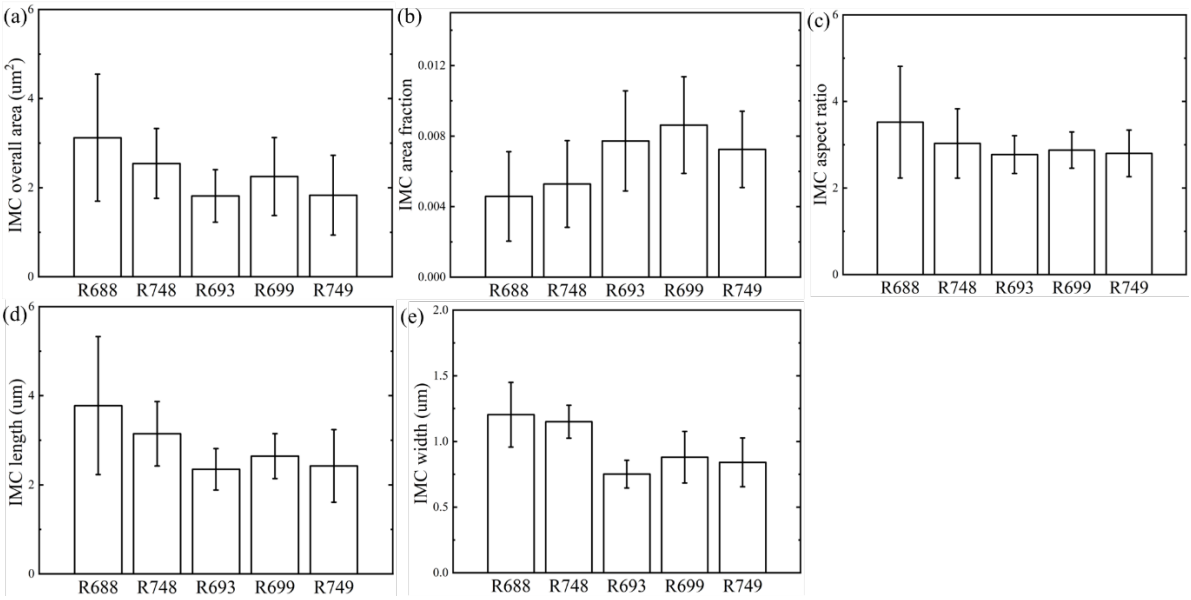


Figure 4.14. Comparison of IMC measurements of all five samples (a) overall area; (b) area fraction; (c) aspect ratio; (d) length; (e) width.

4.1.2 Wedge-casting microstructure

Fig 4.15 shows SEM micrographs of the wedge-cast 4043 Al alloy at five positions from tip a to heel d. The microstructure consists of primary α-Al dendritic/cellular regions, with Al-Si eutectic and Fe-rich IMCs located mainly in the interdendritic regions. From tip to heel, the dendritic structure becomes coarser and the secondary-phase regions appear more widely spaced.

Fig 4.18 shows the measured SDAS at each wedge position and the corresponding derived cooling rates. SDAS increased progressively from tip to heel. At tip a, where the derived cooling rate was 86.61 ± 33.10 K/s, the SDAS was 11.80 ± 2.28 μm. At heel d, where the derived cooling rate was 11.24 ± 4.52 K/s, the SDAS was 23.16 ± 5.61 μm.

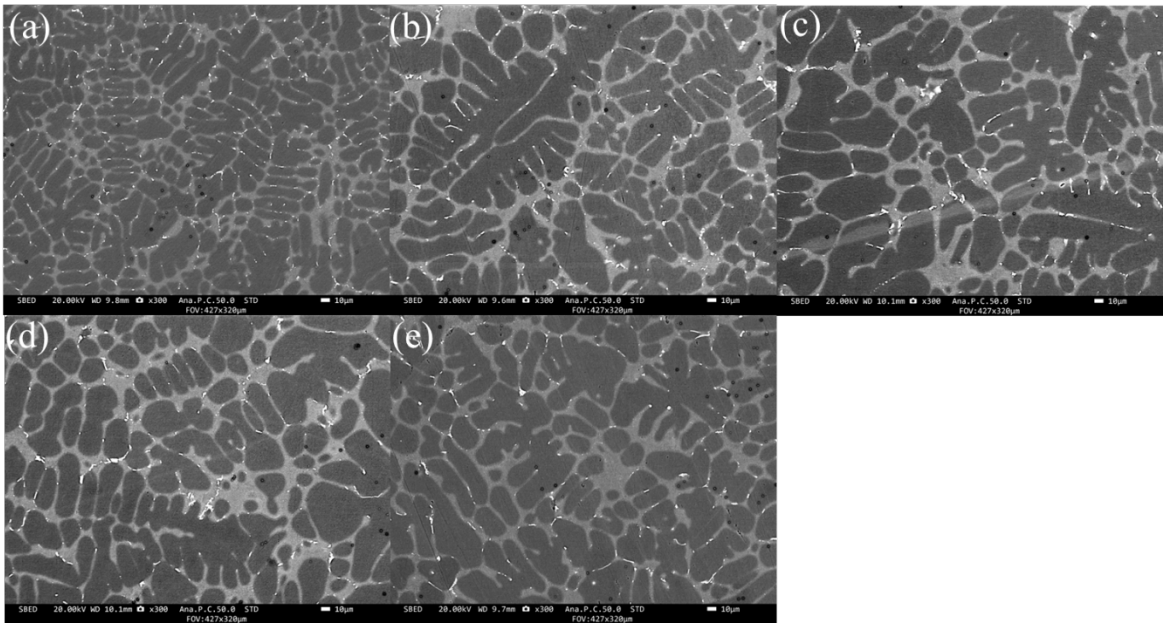


Figure 4.15. SEM images of the wedge-casted 4043 Al alloy showing morphology at five different positions in the wedge with corresponding cooling rate (a) tip a – 86.61 ± 33.10 K/s; (b) tip b – 26.93 ± 7.90 K/s; (c) Middle – 16.20 ± 3.46 K/s; (d) heel c – 11.44 ± 4.91 K/s; (e) heel d – 11.24 ± 4.52 K/s.

Figs 4.19 and 4.20 show the Fe-rich IMC measurements as a function of cooling rate and wedge position, respectively. The average IMC area increased from 2.04 ± 0.29 μm² at tip a to 5.42 ± 0.74 μm² at heel c. The IMC area fraction increased from 0.005 ± 0.002 at tip a to 0.007 ± 0.001 at the middle-top position. The IMC aspect ratio remained close to 2.5 across the measured positions. IMC length and width increased from tip to heel, while IMC number density decreased.

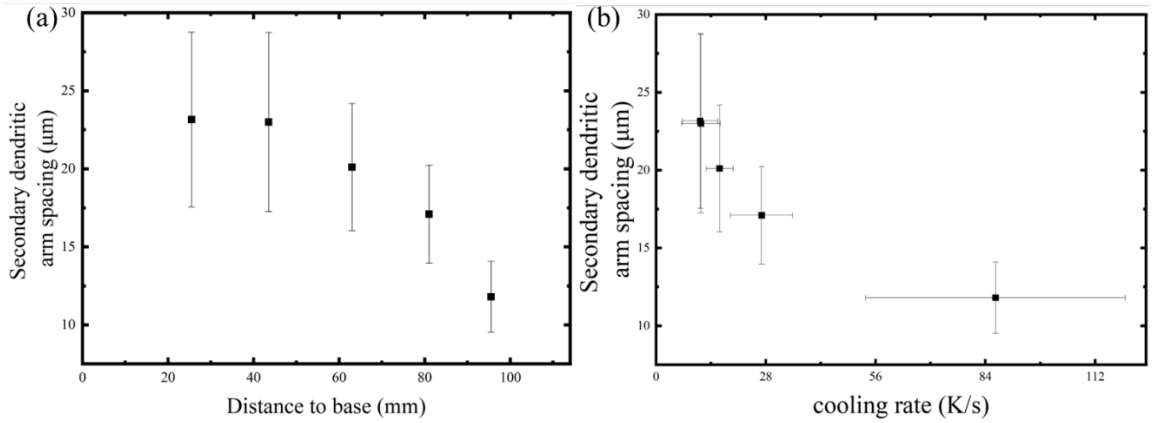


Figure 4.16. SDAS of 4043 Al alloy made by wedge casting (a) SDAS against positions of the wedge; (b) SDAS against cooling rates.

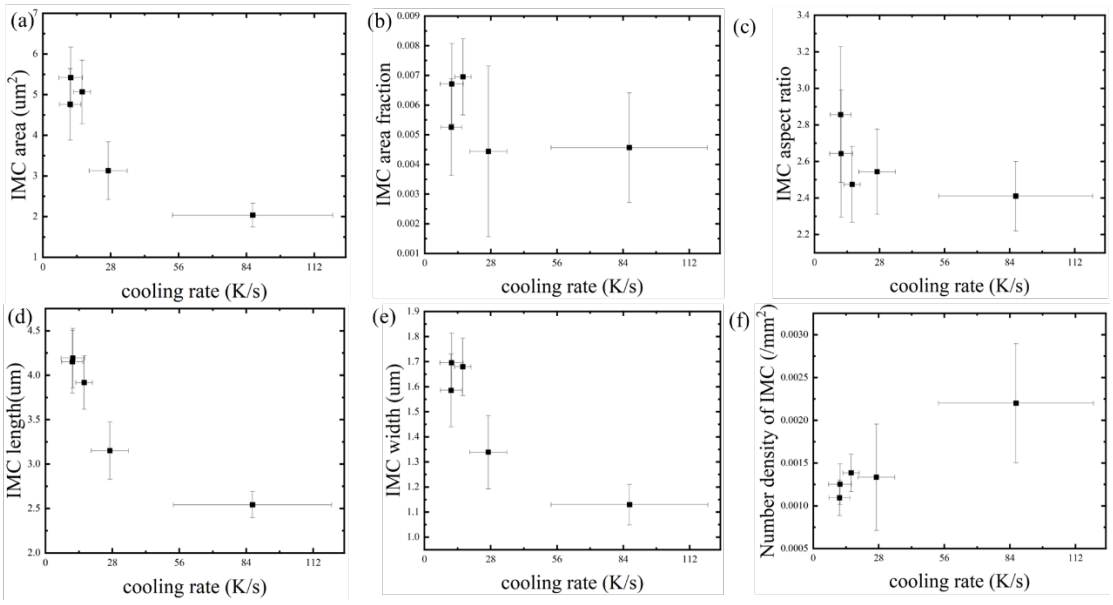


Figure 4.17. IMC measurement against cooling rates (a) IMC area; (b) IMC area fraction; (c) IMC aspect ratio; (d) IMC length; (e) IMC width; (f) IMC number density.

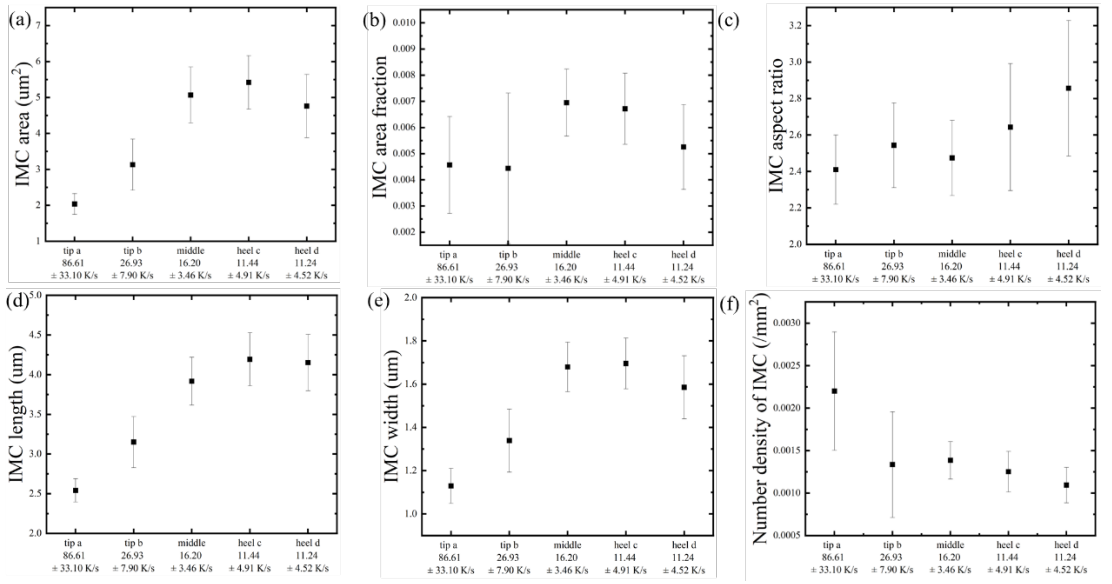


Figure 4.18. IMC measurements against positions in the wedge (a) IMC area; (b) IMC area fraction; (c) IMC aspect ratio; (d) IMC length; (e) IMC width; (f) IMC number density.

4.2 Discussion

4.2.1 Influence of process parameters on layer geometry

The layer-width measurements in Fig 4.2 show that the centre width remained comparatively stable across the five samples, whereas the junction width was more sensitive to both

processing conditions and build height. This difference was most evident in R748 and R688, where the junction width decreased after approximately 40 layers. The centre region is mainly controlled by the volume of deposited material and its immediate spreading after extrusion, while the junction region is more strongly affected by local remelting, wetting and heat transfer at the interface with the previously deposited layer.

Comparison with the processing parameters in Fig 3.3 indicates that R688 and R748 were printed at higher speeds than the other samples. The higher printing speed would reduce the time available for lateral spreading and remelting at the junction, making this region more sensitive to heat loss as the build height increased. This effect was strongest in R748, which was processed with constant and comparatively lower nozzle and substrate temperatures. In R688, the increase in nozzle and substrate temperature during the build appears to have partially compensated for the higher printing speed, resulting in a slightly larger junction width than in R748.

The reduction in junction width after approximately 40 layers is therefore consistent with a progressive reduction in effective heat input at the top surface as the stack moved farther from the heated substrate. In the earlier layers, the deposited material was closer to the substrate and likely experienced more stable thermal conditions, supporting better wetting and spreading at the junction. At greater build heights, heat loss through the growing stack and to the surrounding environment reduced the time available for junction remelting and liquid spreading, leading to narrower junctions.

4.2.2 Influence of process parameters on the microstructure

The results indicate that the overall microstructure was relatively insensitive to the range of printing conditions investigated. Although the five builds were produced using different combinations of printing speed, nozzle temperature and substrate temperature, they all retained

a similar dendritic α-Al matrix with interdendritic Al-Si eutectic and fine Fe-rich IMCs. This suggests that the investigated process window produced a broadly reproducible microstructure. The α-Al grains were comparatively isotropic, with no clear evidence of the strongly elongated columnar structures commonly reported for laser-based AM processes. For comparison, Knapp et al. reported that laser wire AM of the same 4043 alloy produced an as-printed microstructure with an average α-Al grain length of 728 ± 386 µm, grain width of 157 ± 113 µm and aspect ratio of 5 ± 2. In the present MMD samples, the measured grains were much finer and less elongated: R748 had an average α-Al grain length of 62 ± 43 µm, width of 31 ± 21 µm and aspect ratio of 2 ± 1, while R688 had an average length of 69 ± 47 µm, width of 37 ± 27 µm and aspect ratio of 2 ± 1.

The main microstructural variation was associated with build height rather than a change in the fundamental phase morphology. The measured SDAS in Fig 4.10 and the grain-size distributions in Figs 4.8 and 4.9 show that the α-Al scale changed from layer to layer: SDAS and grain size increased during the early stages of the build and then decreased towards the upper layers. This trend reflects the changing thermal history during deposition, where early heat accumulation and subsequent heat loss with increasing build height alter the local solidification conditions.

The centre and junction regions contained the same main phases, namely primary α-Al, Al-Si eutectic and Fe-rich IMCs, but differed in the local distribution of eutectic/Si-rich regions. Local eutectic enrichment was observed at the junctions, consistent with partial remelting and resolidification of low-melting interdendritic regions during layer deposition. These enriched regions remained localised and did not form a continuous macroscopic discontinuity, while the α-Al dendritic structure remained continuous across the junctions. A small but consistent reduction in grain size or SDAS, by approximately 2-3 µm, was also observed at the junctions, indicating a slightly finer local dendritic structure than in the centre regions. This may reflect

a shorter local remelting-resolidification cycle at the junction, where contact with previously solidified material promotes efficient heat extraction after wetting.

Across all samples, the Fe-rich IMCs remained fine and discontinuous, with only modest changes in size, aspect ratio and area fraction. Fig 4.11 shows that the variation in IMC size and length with build height broadly followed the SDAS evolution shown in Fig 4.10. This is consistent with the IMCs forming as secondary phases during the final stages of solidification, mainly within the interdendritic channels. The IMC aspect ratio followed a similar trend to particle size in the samples printed at higher speed, whereas it remained comparatively stable in the other samples. Overall, the Fe-rich IMCs had median lengths between 2 and 4 μm, with 95% of the measured particles shorter than 10 μm. The aspect ratio was also relatively stable, with a median close to 3 and a 95th percentile below 10, indicating that the IMCs remained refined rather than developing into coarse, elongated plate-like particles.

4.2.3 Comparison with L-PBF and wedge casting

Fig 4.22 compares the MMD microstructure with an Al-Si alloy processed by L-PBF. In L-PBF, powder is locally melted by a moving laser heat source, producing overlapping melt pools whose boundaries are visible as curved scan-track features in Fig 4.22(b) and (d). By contrast, the MMD microstructure appears more continuous, with no pronounced melt-pool boundaries in the regions shown in Fig 4.22(a) and (c), consistent with the junction and centre microstructures shown in Figs 4.5 and 4.6. The L-PBF sample shows a more directional microstructure, with columnar grains aligned with the local thermal gradient and scan direction, whereas the MMD sample shows a finer and more equiaxed α-Al grain structure.

The distribution of secondary phases also differs between the two processes. In L-PBF, stronger segregation is observed at melt-pool boundaries, where repeated remelting and resolidification can concentrate solute elements such as Si and Fe. These elements are rejected from the α-Al

matrix during solidification and can accumulate along pool boundaries, producing the streak-like features visible in Fig 4.22(b). In MMD, the feedstock is melted and cast continuously, and solidification appears less strongly directional. Fe-rich IMCs are therefore more uniformly dispersed across the deposited layers, and the grain structure is less columnar. This comparison supports the previous observation that MMD produces a microstructure closer to a fine cast Al-Si alloy than to the highly directional columnar structures often reported in laser-based AM processes.

The similarity between MMD and wedge casting is mainly reflected in the comparable SDAS values and the cooling-rates. In wedge casting, the cooling rate decreases progressively from the tip to the heel because of the mould geometry, producing coarser α-Al dendrites and larger Fe-rich IMCs at lower cooling rates, as shown in Figs 4.15, 4.18 and 4.19. In MMD, the solidification conditions vary with build height because of changes in printing speed, nozzle temperature, substrate temperature and heat loss through the growing stack. Although the thermal histories are different, both processes provide a range of cooling conditions that can be compared through SDAS and IMC morphology.

Using cooling rates estimated from SDAS measurements in Figs 4.10 and 4.18, the microstructures formed at different MMD build heights can be related to corresponding positions in the wedge-cast ingot. At comparable cooling rates, the Fe-rich IMCs show similar trends in area, aspect ratio, length and width, as shown by the MMD and wedge-cast measurements in Figs 4.11, 4.14, 4.19 and 4.20. In both processes, higher cooling rates are associated with finer IMCs, whereas lower cooling rates are associated with coarser and more elongated particles. The measured SDAS values further support this comparison: MMD produced a median SDAS of 17 µm and a 95th percentile of 33 µm, while wedge casting produced a median SDAS of 18 µm and a 95th percentile of 31 µm.

Overall, the comparison shows that the MMD microstructure differs from L-PBF because it lacks strong melt-pool boundary contrast and highly directional columnar grains. Instead, its dendritic α-Al morphology, SDAS range and Fe-rich IMC characteristics are closer to those observed in the wedge-cast 4043 alloy shown in Fig 4.15, although MMD also shows local junction enrichment associated with layer-by-layer remelting and resolidification.

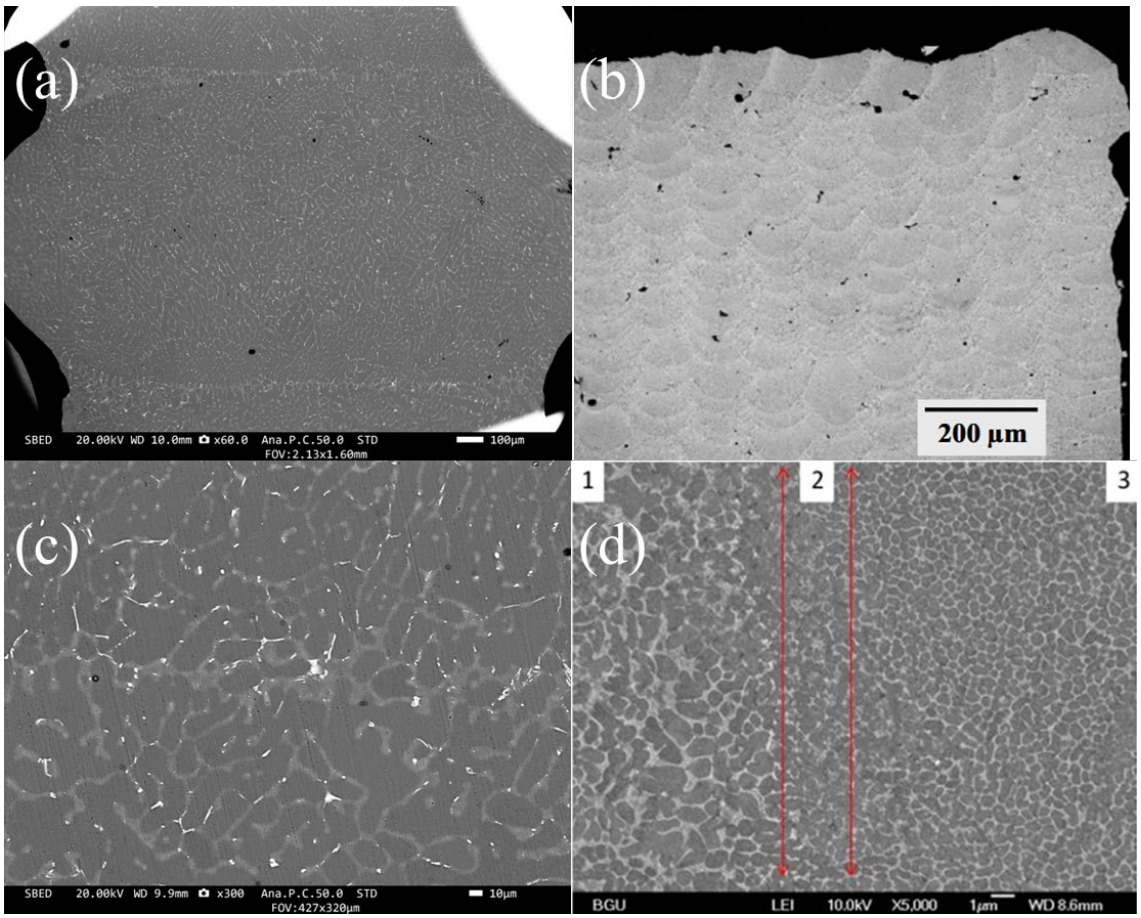


Figure 4.19. Comparison between microstructures of cross-sections produced by MMD and L-PBF (a)(c) as-manufactured 4043 sample by MMD; (b)(d) AlSi10Mg by L-PBF [1], [2].

Chapter 5

Conclusions

This work investigated the microstructural evolution of 4043 Al alloy manufactured by molten metal deposition (MMD) under different combinations of printing speed, nozzle temperature and substrate temperature. SEM observations, quantitative image analysis, grain-size measurements and secondary dendrite arm spacing (SDAS) analysis were used to evaluate layer geometry, junction formation, α-Al morphology and Fe-rich intermetallic compound (IMC) characteristics. A wedge-cast 4043 Al alloy was also analysed to provide a cooling-rate reference for interpreting the solidification conditions produced during MMD.

The MMD samples produced a relatively continuous dendritic α-Al microstructure containing fine interdendritic Al-Si eutectic and discontinuous Fe-rich IMCs. Across the investigated process window, the fundamental phase morphology remained broadly similar. The α-Al grains were comparatively isotropic, with no clear evidence of the strongly elongated columnar structures commonly reported for laser-based AM processes. Local Si / eutectic enrichment was observed at interlayer junctions, consistent with the anticipation on the influence of partial remelting and resolidification during layer deposition, but these enriched regions remained localised and did not form a continuous macroscopic discontinuity through the build.

The main process-related variation was observed in the layer geometry and in the scale of the solidification structure, rather than in a change in the type of microstructure formed. The centre width remained comparatively stable across the five MMD samples, whereas the junction width was more sensitive to build height and processing conditions. This was most evident in the

higher-speed builds, R688 and R748, where the junction width decreased after approximately 40 layers. This behaviour is consistent with a reduction in effective heat input and reduced time for remelting, wetting and lateral spreading at greater build heights.

Grain-size and SDAS measurements showed that the microstructural scale varied through the build. In most samples, SDAS increased during the early stages of deposition and then decreased towards the upper layers, indicating that the local solidification conditions evolved with build height. The Fe-rich IMCs remained fine and discontinuous across all samples, with median lengths generally in the range of a few micrometres. Their size and morphology broadly followed the SDAS evolution: lower cooling rates were associated with coarser and more elongated IMCs, whereas higher cooling rates produced finer and more compact particles.

The wedge-cast 4043 Al alloy confirmed the effect of cooling rate on the Al-Si dendritic structure and Fe-rich IMC morphology. From the tip to the heel of the wedge, the derived cooling rate decreased, SDAS increased, and the Fe-rich IMCs became larger while their number density decreased. These trends were consistent with the MMD observations when both processes were compared using cooling rates estimated from SDAS. Although MMD and wedge casting have different thermal histories and geometries, the comparison shows that cooling rate is a key factor controlling IMC size and morphology under the conditions investigated.

Overall, the results show that MMD can produce a relatively homogeneous, near-isotropic 4043 Al alloy microstructure with limited melt-pool-like boundary contrast and refined Fe-rich IMCs. The process is therefore distinct from laser-based powder-bed AM, where steep thermal gradients and overlapping melt pools often promote stronger columnar grain growth and melt-

pool boundary segregation. The wedge-casting comparison provides a useful framework for interpreting MMD microstructural evolution in terms of cooling rate, supporting future optimisation of process parameters for Al alloys.

Chapter 6

Further work

This thesis has shown that MMD can produce a relatively homogeneous 4043 aluminium alloy microstructure, characterised by near-isotropic α-Al grains, localised solute enrichment at interlayer junctions and refined IMCs. However, the study was limited to a single commercial Al-Si alloy and a selected processing window.

Further work should therefore extend the range of alloys and processing conditions investigated, while also linking the measured microstructural features to mechanical performance and in-service behaviour. Possible directions for future research include:

- *Extension to other aluminium alloy systems*. Other commercially important aluminium alloys, particularly 6xxx and 7xxx series alloys, should be investigated. These alloys are widely used in structural applications because of their precipitation-hardening response, but they are also more compositionally complex than 4043 and may be more sensitive to cracking, segregation and loss of mechanical performance during AM. Applying the same approach used in this work to 6xxx and 7xxx alloys would make it possible to determine whether MMD could retain a similarly homogeneous, near-isotropic microstructure when higher levels of Mg, Si, Zn, Cu and other solute elements are present.
- *Recycled and low-grade scrap feedstock*. A second important direction is to investigate recycled aluminium alloys produced from low-grade scrap. Low-grade scrap streams often contain elevated Fe and other impurity elements that are difficult to remove economically. Since Fe-rich IMCs were the main secondary phases quantified in this work, MMD offers a useful platform for studying how recycled feedstock chemistry

affects IMC formation, morphology and distribution during layer-by-layer solidification.

- *Wider processing window and thermal control*. Further work should also extend the process window, especially towards higher printing speeds. The present results showed that the centre width was relatively stable, while the junction width was more sensitive to build height and processing conditions, particularly in the higher-speed samples. A wider range of printing speeds would clarify the limits of stable deposition and identify when insufficient wetting, reduced remelting or excessive heat loss begins to compromise junction consistency. Nozzle temperature and substrate temperature should be varied systematically together with printing speed. This would allow the effect of thermal input on junction width, layer morphology and SDAS to be separated more clearly. In particular, future experiments should determine whether active control of nozzle and substrate temperature can compensate for the reduction in effective heat input at larger build heights.

- Electron Backscatter Diffraction (EBSD)

  EBSD can be utilized for the microstructural feature measurements below and more methods of employment are in consideration:

1. Visualize the morphology, size, and distribution of grains, subgrains, or phases using orientation contrast imaging. For MMD-processed samples, the size and distribution of equiaxed and columnar grains can be measured.
2. Investigate the distribution of grain misorientations and their evolution during deformation. The orientation of columnar grains often observed near the junction region can be identified for analysis of thermal gradient in solidification of MMD process.

3. Perform phase identification and phase content analysis; and qualitatively analyze crystal defects based on Kikuchi pattern quality. For MMD-processed samples, identification of various types of IMCs can be further confirmed. And, proliferation of dislocation can be recorded for subsequent plasticity test.

- EDX

  1. IMCs

  Types of IMCs could be identified based on diffracted X-ray signal of different elements. α-Al_8Fe_2Si consists of higher content of Fe than that of β-Al_5FeSi, thus α-phase will show a higher intensity of Fe signal. Combined with identification of morphological difference, IMC types could be confirmed.

  2. Alloy composition

  EDX will produce elemental qualification and quantification in field of view (FOV) which offers additional information on phase distribution and interdentritic channel width.

- Mechanical testing

The junction regions of 4043 Al alloy processed by MMD mainly consist of eutectic Si which coexisted with IMCs. It can be observed on the SEM images that junction contains a high IMC concentration. Especially, with detrimental effects of β-IMCs on mechanical performance, mechanical tests could be vital. Two mechanical tests of interests are listed below:

1. Plasticity test by elongation along build direction at various increment.

2. Fracture toughness tests by employing shear stresses on specifically-selected junciton regions to estimate the variance in flexural strength along increasing stack height.

Chapter 9

Bibliography

[1] I. Rosenthal, A. Stern, and N. Frage, 'Microstructure and Mechanical Properties of AlSi10Mg Parts Produced by the Laser Beam Additive Manufacturing (AM) Technology', *Metallogr. Microstruct. Anal.*, vol. 3, no. 6, pp. 448–453, Dec. 2014, doi: 10.1007/s13632-014-0168-y.

[2] L. Thijs, K. Kempen, J.-P. Kruth, and J. Van Humbeeck, 'Fine-structured aluminium products with controllable texture by selective laser melting of pre-alloyed AlSi10Mg powder', *Acta Materialia*, vol. 61, no. 5, pp. 1809–1819, Mar. 2013, doi: 10.1016/j.actamat.2012.11.052.

[3] W. E. Frazier, 'Metal Additive Manufacturing: A Review', *J. of Materi Eng and Perform*, vol. 23, no. 6, pp. 1917–1928, Jun. 2014, doi: 10.1007/s11665-014-0958-z.

[4] H. R. Kotadia, G. Gibbons, A. Das, and P. D. Howes, 'A review of Laser Powder Bed Fusion Additive Manufacturing of aluminium alloys: Microstructure and properties', *Additive Manufacturing*, vol. 46, p. 102155, Oct. 2021, doi: 10.1016/j.addma.2021.102155.

[5] J. Hirsch, 'Aluminium in Innovative Light-Weight Car Design', *Mater. Trans.*, vol. 52, no. 5, pp. 818–824, 2011, doi: 10.2320/matertrans.L-MZ201132.

[6] A. Bouzekova-Penkova and A. Miteva, 'Some Aerospace Applications of 7075 (B95) Aluminium Alloy', *ARB*, vol. 34, pp. 165–179, 2022, doi: 10.3897/arb.v34.e15.

[7] S. K. Manjhi, B. S. S. Kumar, J. P. Rodrigues, P. Sekar, S. Bontha, and A. S. S. Balan, 'An Experimental Investigation on Microstructure, Mechanical Properties and Corrosion Performance of CMT-Wire Arc Additively Manufactured Al-4043 Alloy', *Trans Indian Inst Met*, vol. 76, no. 10, pp. 2745–2756, Oct. 2023, doi: 10.1007/s12666-023-02965-7.

[8] C. Menapace, J. Galle, C. Elangeswaran, and A. Makaya, 'Production and Characterization of Al Alloys Obtained Through Molten Metal Deposition', *Metals*, vol. 16, no. 2, p. 238, Feb. 2026, doi: 10.3390/met16020238.

[9] E. Hoekstra *et al.*, 'Additive Manufacturing of an Aluminium Alloy by Molten Metal Deposition: A Finite Element and Experimental Study', Dec. 28, 2024, *Social Science Research Network, Rochester, NY*: 5074770. doi: 10.2139/ssrn.5074770.

[10] A. Kapil, V. Sharma, J. D. Pauw, and A. Sharma, 'Exploring impact, spreading, and bonding dynamics in molten metal deposition for novel drop-on-demand printing', *Materials & Design*, vol. 238, p. 112633, Feb. 2024, doi: 10.1016/j.matdes.2024.112633.

[11] Z. Zhu *et al.*, 'Recent progress on the additive manufacturing of aluminum alloys and aluminum matrix composites: Microstructure, properties, and applications', *International Journal of Machine Tools and Manufacture*, vol. 190, p. 104047, Aug. 2023, doi: 10.1016/j.ijmachtools.2023.104047.

[12] D. Zhang *et al.*, 'Grain Refinement of Alloys in Fusion-Based Additive Manufacturing Processes', *Metall Mater Trans A*, vol. 51, no. 9, pp. 4341–4359, Sep. 2020, doi: 10.1007/s11661-020-05880-4.

[13] N. Tuncer and A. Bose, 'Solid-State Metal Additive Manufacturing: A Review', *JOM*, vol. 72, no. 9, pp. 3090–3111, Sep. 2020, doi: 10.1007/s11837-020-04260-y.

[14] J. P. Oliveira, T. G. Santos, and R. M. Miranda, ‘Revisiting fundamental welding concepts to improve additive manufacturing: From theory to practice’, *Progress in Materials Science*, vol. 107, p. 100590, Jan. 2020, doi: 10.1016/j.pmatsci.2019.100590.
[15] D. Herzog, V. Seyda, E. Wycisk, and C. Emmelmann, ‘Additive manufacturing of metals’, *Acta Materialia*, vol. 117, pp. 371–392, Sep. 2016, doi: 10.1016/j.actamat.2016.07.019.
[16] S. Ashley, ‘Rapid Prototyping Systems’, *Mechanical Engineering*, vol. 113, no. 4, American Society of Mechanical Engineers, New York, United States, p. 34, Apr. 1991.
[17] K. V. Wong and A. Hernandez, ‘A Review of Additive Manufacturing’, *International Scholarly Research Notices*, vol. 2012, no. 1, p. 208760, 2012, doi: 10.5402/2012/208760.
[18] J. J. Beaman, D. L. Bourell, C. C. Seepersad, and D. Kovar, ‘Additive Manufacturing Review: Early Past to Current Practice’, *J. Manuf. Sci. Eng*, vol. 142, no. 110812, Sep. 2020, doi: 10.1115/1.4048193.
[19] J. R. Davis, *Aluminum and Aluminum Alloys*. ASM International, 1993.
[20] T. DebRoy *et al.*, ‘Additive manufacturing of metallic components – Process, structure and properties’, *Progress in Materials Science*, vol. 92, pp. 112–224, Mar. 2018, doi: 10.1016/j.pmatsci.2017.10.001.
[21] Z. Li *et al.*, ‘High deposition rate powder- and wire-based laser directed energy deposition of metallic materials: A review’, *International Journal of Machine Tools and Manufacture*, vol. 181, p. 103942, Oct. 2022, doi: 10.1016/j.ijmachtools.2022.103942.
[22] A. Mostafaei *et al.*, ‘Binder jet 3D printing—Process parameters, materials, properties, modeling, and challenges’, *Progress in Materials Science*, vol. 119, p. 100707, Jun. 2021, doi: 10.1016/j.pmatsci.2020.100707.
[23] M. Krinitcyn, N. Toropkov, A. Pervikov, and M. Lerner, ‘Structure and mechanical properties of Fe-10Cu alloy obtained by material extrusion-based additive manufacturing method with bimodal powder’, *Powder Technology*, vol. 406, p. 117593, Jul. 2022, doi: 10.1016/j.powtec.2022.117593.
[24] M. Jurisch, T. Studnitzky, O. Andersen, and B. Kieback, ‘3D Screen Printing – Additive Manufacturing of Finely Structured Titanium Based Parts’.
[25] R. R. Dehoff and S. S. Babu, ‘Characterization of interfacial microstructures in 3003 aluminum alloy blocks fabricated by ultrasonic additive manufacturing’, *Acta Materialia*, vol. 58, no. 13, pp. 4305–4315, Aug. 2010, doi: 10.1016/j.actamat.2010.03.006.
[26] ‘Full article: Additive friction stir deposition: a deformation processing route to metal additive manufacturing’. Accessed: Sep. 07, 2025. [Online]. Available: https://www.tandfonline.com/doi/full/10.1080/21663831.2020.1847211
[27] L. Ajdelsztajn, J. M. Schoenung, B. Jodoin, and G. E. Kim, ‘Cold spray deposition of nanocrystalline aluminum alloys’, *Metall Mater Trans A*, vol. 36, no. 3, pp. 657–666, Mar. 2005, doi: 10.1007/s11661-005-0182-4.
[28] G. L. Knapp, M. Gussev, A. Shyam, T. Feldhausen, and A. Plotkowski, ‘Microstructure, deformation and fracture mechanisms in Al-4043 alloy produced by laser hot-wire additive manufacturing’, *Additive Manufacturing*, vol. 59, p. 103150, Nov. 2022, doi: 10.1016/j.addma.2022.103150.
[29] E. O. Olakanmi, R. F. Cochrane, and K. W. Dalgarno, ‘A review on selective laser sintering/melting (SLS/SLM) of aluminium alloy powders: Processing, microstructure, and properties’, *Progress in Materials Science*, vol. 74, pp. 401–477, Oct. 2015, doi: 10.1016/j.pmatsci.2015.03.002.
[30] J. R. Croteau *et al.*, ‘Microstructure and mechanical properties of Al-Mg-Zr alloys processed by selective laser melting’, *Acta Materialia*, vol. 153, pp. 35–44, Jul. 2018, doi: 10.1016/j.actamat.2018.04.053.
[31] A. Kapil, V. Sharma, J. D. Pauw, and A. Sharma, ‘A novel molten metal deposition-based additive manufacturing technique for aluminum alloys’, 2023.

[32] E. Hoekstra *et al.*, 'Additive manufacturing of Al-4043 by molten metal deposition: coupled thermal modeling and microstructural characterization', *Prog Addit Manuf*, May 2026, doi: 10.1007/s40964-026-01727-3.
[33] J. H. Martin, B. D. Yahata, J. M. Hundley, J. A. Mayer, T. A. Schaedler, and T. M. Pollock, '3D printing of high-strength aluminium alloys', *Nature*, vol. 549, no. 7672, pp. 365–369, Sep. 2017, doi: 10.1038/nature23894.
[34] N. M. Siddesh Kumar, Dhruthi, G. K. Pramod, P. Samrat, and M. Sadashiva, 'A Critical Review on Heat Treatment of Aluminium Alloys', *Materials Today: Proceedings*, vol. 58, pp. 71–79, Jan. 2022, doi: 10.1016/j.matpr.2021.12.586.
[35] T. DebRoy *et al.*, 'Additive manufacturing of metallic components – Process, structure and properties', *Progress in Materials Science*, vol. 92, pp. 112–224, Mar. 2018, doi: 10.1016/j.pmatsci.2017.10.001.
[36] D. Herzog, V. Seyda, E. Wycisk, and C. Emmelmann, 'Additive manufacturing of metals', *Acta Materialia*, vol. 117, pp. 371–392, Sep. 2016, doi: 10.1016/j.actamat.2016.07.019.
[37] T. G. Holesinger *et al.*, 'Characterization of an Aluminum Alloy Hemispherical Shell Fabricated via Direct Metal Laser Melting', *JOM*, vol. 68, no. 3, pp. 1000–1011, Mar. 2016, doi: 10.1007/s11837-015-1798-5.
[38] M. Wang, B. Song, Q. Wei, Y. Zhang, and Y. Shi, 'Effects of annealing on the microstructure and mechanical properties of selective laser melted AlSi7Mg alloy', *Materials Science and Engineering: A*, vol. 739, pp. 463–472, Jan. 2019, doi: 10.1016/j.msea.2018.10.047.
[39] N. Read, W. Wang, K. Essa, and M. M. Attallah, 'Selective laser melting of AlSi10Mg alloy: Process optimisation and mechanical properties development', *Materials & Design (1980-2015)*, vol. 65, pp. 417–424, Jan. 2015, doi: 10.1016/j.matdes.2014.09.044.
[40] L. Zhuo *et al.*, 'Effect of post-process heat treatment on microstructure and properties of selective laser melted AlSi10Mg alloy', *Materials Letters*, vol. 234, pp. 196–200, Jan. 2019, doi: 10.1016/j.matlet.2018.09.109.
[41] K. G. Prashanth *et al.*, 'Microstructure and mechanical properties of Al–12Si produced by selective laser melting: Effect of heat treatment', *Materials Science and Engineering: A*, vol. 590, pp. 153–160, Jan. 2014, doi: 10.1016/j.msea.2013.10.023.
[42] X. P. Li *et al.*, 'A selective laser melting and solution heat treatment refined Al–12Si alloy with a controllable ultrafine eutectic microstructure and 25% tensile ductility', *Acta Materialia*, vol. 95, pp. 74–82, Aug. 2015, doi: 10.1016/j.actamat.2015.05.017.
[43] N. Kang, P. Coddet, C. Chen, Y. Wang, H. Liao, and C. Coddet, 'Microstructure and wear behavior of *in-situ* hypereutectic Al–high Si alloys produced by selective laser melting', *Materials & Design*, vol. 99, pp. 120–126, Jun. 2016, doi: 10.1016/j.matdes.2016.03.053.
[44] P. Ma *et al.*, 'Influence of Annealing on Mechanical Properties of Al-20Si Processed by Selective Laser Melting', *Metals*, vol. 4, no. 1, pp. 28–36, Mar. 2014, doi: 10.3390/met4010028.
[45] Q. Tan *et al.*, 'Inoculation treatment of an additively manufactured 2024 aluminium alloy with titanium nanoparticles', *Acta Materialia*, vol. 196, pp. 1–16, Sep. 2020, doi: 10.1016/j.actamat.2020.06.026.
[46] F. Belelli, R. Casati, F. Larini, M. Riccio, and M. Vedani, 'Investigation on two Ti–B-reinforced Al alloys for Laser Powder Bed Fusion', *Materials Science and Engineering: A*, vol. 808, p. 140944, Mar. 2021, doi: 10.1016/j.msea.2021.140944.
[47] G. P. Dinda, A. K. Dasgupta, and J. Mazumder, 'Evolution of microstructure in laser deposited Al–11.28%Si alloy', *Surface and Coatings Technology*, vol. 206, no. 8, pp. 2152–2160, Jan. 2012, doi: 10.1016/j.surfcoat.2011.09.051.

[48] Q. Jia, P. Rometsch, S. Cao, K. Zhang, and X. Wu, 'Towards a high strength aluminium alloy development methodology for selective laser melting', *Materials & Design*, vol. 174, p. 107775, Jul. 2019, doi: 10.1016/j.matdes.2019.107775.
[49] S. Z. Uddin, L. E. Murr, C. A. Terrazas, P. Morton, D. A. Roberson, and R. B. Wicker, 'Processing and characterization of crack-free aluminum 6061 using high-temperature heating in laser powder bed fusion additive manufacturing', *Additive Manufacturing*, vol. 22, pp. 405–415, Aug. 2018, doi: 10.1016/j.addma.2018.05.047.
[50] 'New Aluminum Alloys Specifically Designed for Laser Powder Bed Fusion: A Review'. Accessed: Jun. 18, 2026. [Online]. Available: https://www.mdpi.com/1996-1944/12/7/1007
[51] J. R. Croteau *et al.*, 'Microstructure and mechanical properties of Al-Mg-Zr alloys processed by selective laser melting', *Acta Materialia*, vol. 153, pp. 35–44, Jul. 2018, doi: 10.1016/j.actamat.2018.04.053.
[52] J. R. Croteau *et al.*, 'Microstructure and mechanical properties of Al-Mg-Zr alloys processed by selective laser melting', *Acta Materialia*, vol. 153, pp. 35–44, Jul. 2018, doi: 10.1016/j.actamat.2018.04.053.
[53] N. Tuncer and A. Bose, 'Solid-State Metal Additive Manufacturing: A Review', *JOM*, vol. 72, no. 9, pp. 3090–3111, Sep. 2020, doi: 10.1007/s11837-020-04260-y.
[54] A. Tonejc, 'X-ray study of the decomposition of metastable Al-rich Al-Fe solid solutions', *MT*, vol. 2, no. 2, pp. 437–440, 1971, doi: 10.1007/BF02663331.
[55] J. L. Murray and A. J. McAlister, 'The Al-Si (Aluminum-Silicon) system', *Bulletin of Alloy Phase Diagrams*, vol. 5, no. 1, pp. 74–84, Feb. 1984, doi: 10.1007/BF02868729.
[56] L. E. Murr *et al.*, 'Microstructural Architecture, Microstructures, and Mechanical Properties for a Nickel-Base Superalloy Fabricated by Electron Beam Melting', *Metall Mater Trans A*, vol. 42, no. 11, pp. 3491–3508, Nov. 2011, doi: 10.1007/s11661-011-0748-2.
[57] S. G. Lambrakos and K. P. Cooper, 'An Algorithm for Inverse Modeling of Layer-by-Layer Deposition Processes', *J. of Materi Eng and Perform*, vol. 18, no. 3, pp. 221–230, Apr. 2009, doi: 10.1007/s11665-008-9268-7.
[58] S. G. Lambrakos and K. P. Cooper, 'A General Algorithm for Inverse Modeling of Layer-By-Layer Liquid-Metal Deposition', *J. of Materi Eng and Perform*, vol. 19, no. 3, pp. 314–324, Apr. 2010, doi: 10.1007/s11665-009-9497-4.
[59] Y. K. Xiao *et al.*, 'Effect of nano-TiB2 particles on the anisotropy in an AlSi10Mg alloy processed by selective laser melting', *Journal of Alloys and Compounds*, vol. 798, pp. 644–655, Aug. 2019, doi: 10.1016/j.jallcom.2019.05.279.
[60] Q. Tan, Y. Yin, Z. Fan, J. Zhang, Y. Liu, and M.-X. Zhang, 'Uncovering the roles of LaB6-nanoparticle inoculant in the AlSi10Mg alloy fabricated via selective laser melting', *Materials Science and Engineering: A*, vol. 800, p. 140365, Jan. 2021, doi: 10.1016/j.msea.2020.140365.
[61] Q. Tan *et al.*, 'A novel method to 3D-print fine-grained AlSi10Mg alloy with isotropic properties *via* inoculation with LaB6 nanoparticles', *Additive Manufacturing*, vol. 32, p. 101034, Mar. 2020, doi: 10.1016/j.addma.2019.101034.
[62] R. Li, M. Wang, Z. Li, P. Cao, T. Yuan, and H. Zhu, 'Developing a high-strength Al-Mg-Si-Sc-Zr alloy for selective laser melting: Crack-inhibiting and multiple strengthening mechanisms', *Acta Materialia*, vol. 193, pp. 83–98, Jul. 2020, doi: 10.1016/j.actamat.2020.03.060.
[63] K. V. Yang, Y. Shi, F. Palm, X. Wu, and P. Rometsch, 'Columnar to equiaxed transition in Al-Mg(-Sc)-Zr alloys produced by selective laser melting', *Scripta Materialia*, vol. 145, pp. 113–117, Mar. 2018, doi: 10.1016/j.scriptamat.2017.10.021.

[64] M. L. Montero-Sistiaga *et al.*, ‘Changing the alloy composition of Al7075 for better processability by selective laser melting’, *Journal of Materials Processing Technology*, vol. 238, pp. 437–445, Dec. 2016, doi: 10.1016/j.jmatprotec.2016.08.003.
[65] J. DONATELLI, ‘caratterizzazione di componenti realizzati in lega di alluminio tramite additive manufacturing’, Dec. 2024, Accessed: Jun. 05, 2026. [Online]. Available: https://tesi.univpm.it/handle/20.500.12075/20371?mode=simple
[66] J. H. Perepezko and K. Hildal, ‘Analysis of solidification microstructures during wedge-casting’, *Philosophical Magazine*, vol. 86, no. 24, pp. 3681–3701, Aug. 2006, doi: 10.1080/14786430500404116.
[67] A. S. Haselhuhn, P. G. Sanders, and J. M. Pearce, ‘Hypoeutectic Aluminum–Silicon Alloy Development for GMAW-Based 3-D Printing Using Wedge Castings’, *Inter Metalcast*, vol. 11, no. 4, pp. 843–856, Oct. 2017, doi: 10.1007/s40962-017-0133-z.